

4

TECHNICAL REPORT BRL-TR-3014

BRL

AD-A209 550

PLASMA PROPERTIES OF A LARGE-BORE,
ARC-ARMATURE RAILGUN

KEITH A. JAMISON
HENRY S. BURDEN
JOHN D. POWELL

JULY 1989

DTIC
ELECTE
JUL 03 1989
S E D

APPROVED FOR PUBLIC RELEASE; DISTRIBUTION UNLIMITED.

U.S. ARMY LABORATORY COMMAND

BALLISTIC RESEARCH LABORATORY
ABERDEEN PROVING GROUND, MARYLAND

DESTRUCTION NOTICE

Destroy this report when it is no longer needed. DO NOT return it to the originator.

Additional copies of this report may be obtained from the National Technical Information Service, U.S. Department of Commerce, Springfield, VA 22161.

The findings of this report are not to be construed as an official Department of the Army position, unless so designated by other authorized documents.

The use of trade names or manufacturers' names in this report does not constitute indorsement of any commercial product.

REPORT DOCUMENTATION PAGE

Form Approved
OMB No. 0704-0188

1a. REPORT SECURITY CLASSIFICATION UNCLASSIFIED		1b. RESTRICTIVE MARKINGS	
2a. SECURITY CLASSIFICATION AUTHORITY NA		3. DISTRIBUTION/AVAILABILITY OF REPORT APPROVED FOR PUBLIC RELEASE: DISTRIBUTION UNLIMITED.	
2b. DECLASSIFICATION/DOWNGRADING SCHEDULE NA		5. MONITORING ORGANIZATION REPORT NUMBER(S)	
4. PERFORMING ORGANIZATION REPORT NUMBER(S) BRL-TR-3014		7a. NAME OF MONITORING ORGANIZATION	
6a. NAME OF PERFORMING ORGANIZATION US Army Ballistic Research Laboratory	6b. OFFICE SYMBOL (if applicable) SLCBBR-TB-EP	7b. ADDRESS (City, State, and ZIP Code)	
6c. ADDRESS (City, State, and ZIP Code) Aberdeen Proving Ground, MD 21005-5066		9. PROCUREMENT INSTRUMENT IDENTIFICATION NUMBER	
8a. NAME OF FUNDING/SPONSORING ORGANIZATION US Army Ballistic Research Laboratory	8b. OFFICE SYMBOL (if applicable) SLCBBR-D	10. SOURCE OF FUNDING NUMBERS	
8c. ADDRESS (City, State, and ZIP Code) Aberdeen Proving Ground, MD 21005-5066		PROGRAM ELEMENT NO. 62618A	PROJECT NO. AH80
		TASK NO. 00	WORK UNIT ACCESSION NO. 001AJ
11. TITLE (Include Security Classification) (U) Plasma Properties of a Large-Bore, Arc-Armature Railgun			
12. PERSONAL AUTHOR(S) K. A. Jamison, Henry S. Burden and John D. Powell			
13a. TYPE OF REPORT	13b. TIME COVERED FROM _____ TO _____	14. DATE OF REPORT (Year, Month, Day)	15. PAGE COUNT
16. SUPPLEMENTARY NOTATION			
17. COSATI CODES		18. SUBJECT TERMS (Continue on reverse if necessary and identify by block number)	
FIELD 20	GROUP 03	Railgun, Plasma Armature, Electromagnetic Propulsion, Plasma Diagnostics	
19. ABSTRACT (Continue on reverse if necessary and identify by block number) (1dk) Diagnostic measurements on the plasma armature of the large-bore railgun, CHECMATE, have been made for four separate firings. These measurements include time-dependent values of the current, light output, and breech and muzzle voltages. In addition, signals obtained from "B-dot" data are used to infer the armature induction field, current-density profile, and arc length. The measured results are then employed in conjunction with a one-dimensional, steady-state model to calculate properties of the arc which cannot be measured directly. Among the quantities calculated are the armature mass and the temperature and ionization state as a function of position in the arc. As a result of this analysis, it is concluded that the armature mass remains nearly constant and that the arc temperature is somewhat lower than had been expected previously. Both these factors lend some credence to the use of plasma armatures for a wide variety of applications.			
20. DISTRIBUTION/AVAILABILITY OF ABSTRACT <input checked="" type="checkbox"/> UNCLASSIFIED/UNLIMITED <input type="checkbox"/> SAME AS RPT. <input type="checkbox"/> DTIC USERS		21. ABSTRACT SECURITY CLASSIFICATION UNCLASSIFIED	
22a. NAME OF RESPONSIBLE INDIVIDUAL Henry S. Burden		22b. TELEPHONE (Include Area Code) 301/278-4363	22c. OFFICE SYMBOL SLCBBR-TB-EP

ACKNOWLEDGMENT

The results of this investigation were heavily dependent upon the response provided by Maxwell Laboratories; this proved extremely gratifying. The state-of-the-art facility was competently designed and reliably and repetitively provided the shot performance requested. The professional staff gave clear guidance in setting up the operation, unstinting support during its term, and a full and thorough assessment of test parameters after its completion. The technician staff was enthusiastic and cooperative, pliable in the face of changes, and always ready to give the extra measure of help. The entire operation was one characterized by interest and helpfulness. We truly enjoyed every minute of it.

Accession For	
NTIS GRA&I	<input checked="" type="checkbox"/>
DTIC TAB	<input type="checkbox"/>
Unannounced	<input type="checkbox"/>
Justification	
By _____	
Distribution/	
Availability Codes	
Dist	Avail and/or Special
A-1	



TABLE OF CONTENTS

	<u>Page</u>
ACKNOWLEDGMENT	iii
LIST OF FIGURES	vii
LIST OF TABLES	ix
I. INTRODUCTION	1
II. EXPERIMENTAL RESULTS	3
1. Diagnostic Probes	3
2. Measured Quantities	9
3. Data Analysis	23
III. MODEL CALCULATIONS	31
1. Governing Equations	32
2. Results of Calculations	37
IV. CONCLUSIONS AND RECOMMENDATIONS	46
REFERENCES	47
DISTRIBUTION LIST	49

LIST OF FIGURES

<u>Figure</u>	<u>Page</u>
1 Schematic Illustration of CHECMATE Railgun and Power Supply . . .	2
2 Schematic Circuit for Breech and Muzzle Voltage Probes	5
3 Orientation and Voltage Response of B-Dot Coils	6
4 Induction Field and Light Emission Probe Assembly	7
5 Cross Section View of Probe Mounting Location in CHECMATE Barrel Structure	8
6 Schematic Circuit of PIN Diode Light Detectors	10
7 Railgun Current Versus Time Waveforms for Shots 94-97	11
8 Breech and Muzzle Voltage Traces for Shots 95, 96 and 97	13
9 Four Station B-Dot Loop Voltage Signals; Shot 94	14
10 Four Station B-Dot Loop Voltage Signals; Shot 95	15
11 Four Station B-Dot Loop Voltage Signals; Shot 96	16
12 Four Station B-Dot Loop Voltage Signals; Shot 97	17
13 Light Intensity Versus Time Traces from Four Probes; Shot 95 . .	19
14 Light Intensity Versus Time Traces from Four Probes; Shot 96 . .	20
15 Ideal and Interpolated Accelerations for CHECMATE Railgun Shots 94 and 96	21
16 Ideal and Interpolated Accelerations for CHECMATE Railgun Shots 95 and 97	22
17 Parametric Description of Armature Current Density Function . . .	25
18 Sample Distribution of the Arc Current Density at Four Different Times; Shot 94	27
19 Armature Length Versus Armature Current	28
20 Comparison of Current Density and Light Emission; Shot 95	29
21 Comparison of Current Density and Light Emission; Shot 96	30
22 Calculated Armature Mass Versus Time of the Carbon Arc	38
23 Peak Temperature Versus Current for Carbon Arc	39

LIST OF FIGURES

<u>Figure</u>		<u>Page</u>
24	Average Temperature Versus Current for Carbon Arc	40
25	Average Ion Concentration Versus Current for Carbon Arc	41
26	Comparison of Temperature Profiles for Carbon Arc from Data Analysis and Theory	43
27	Neutral Concentration Averaged Over Trailing Edge of Carbon Arc .	45
28	Armature Mass Versus Time for Different Arc Materials	47
29	Mean Arc Temperature Versus Time for Different Arc Materials . .	48

I. INTRODUCTION

The possible applications of railguns for military uses have been given considerable attention in recent years. Of the many classes of electric guns, the simple linear railgun has received the most study. Within this class, by far the most successful has been the plasma armature type exemplified by the CHECMATE railgun.¹ In this device, a thin aluminum foil on the rear face of the projectile is subjected to a large current and rapidly vaporizes. That current is initiated in the circuit, which includes a substantial inductor, by the discharge of a capacitor. At the instant of complete discharge, the capacitor is then shunted out of the circuit by a low resistance "crowbar". Driven by the energy stored in the field around the inductor, the current continues to flow through the vapor left by the explosion of the foil, heating and ionizing it to produce an arc or plasma. The driving force applied to the projectile arises from the pressure accrued in the gaseous plasma as the diffuse current of density J flowing through it from rail to rail reacts with the accompanying, intense magnetic induction field, B . The term plasma (or, alternatively, arc) implies a hot, ionized, highly luminescent, gaseous conduction path for the railgun current; the term armature relates to the motive part of an electric motor. While the exact environment between the rails behind the projectile is not known in great detail, several theoretical descriptions²⁻⁵ of its state have been offered and numerous experimental studies have been performed on various small railguns.

Most of the projected uses of railguns do not involve small devices, but rather railguns whose bore dimensions are several centimeters and whose lengths are several meters. The CHECMATE railgun has a square bore 5 cm by 5 cm and a length of five meters. It has been used to fire projectiles having masses between 100 and 350 grams at velocities between one and three kilometers per second. At the time of this writing, it has been fired nearly 100 times. The successful operation of the CHECMATE railgun represents a significant advance toward practical applications of railgun technology. A schematic illustration of the railgun and its power supply are shown in Fig. 1.

In this report, we describe a set of diagnostic measurements made on the CHECMATE railgun in an attempt to quantify some of the properties of the plasma arc armature. In addition, these measurements are used in conjunction with a

¹Holland, M.M., Wilkinson, G.M., Krickhuhn, A.P, and Dethlefsen, R., "Six Megajoule Rail Gun Test Facility," IEEE Trans. Magn. MAG-22, 1521 (1986).

²Powell, John D. and Batteh, Jad H., "Plasma Dynamics of an Arc-Driven Electromagnetic Projectile Accelerator," J. Appl. Phys. 52, 2717 (1981). See also, "Plasma Dynamics of the Arc-Driven Rail Gun," Ballistic Research Laboratory Report No. ARBRL-TR-02267, September 1980.

³Powell, John D. and Batteh, Jad H., "Two-Dimensional Plasma Model for the Arc-Driven Railgun," J. Appl. Phys. 54, 2242 (1983). See also Powell, John D., "Two Dimensional Model for Arc Dynamics in the Railgun," Ballistic Research Laboratory Report No. ARBRL-TR-02423, October 1982

⁴Sloan, M.L, "Physics of Rail Gun Plasma Armatures," IEEE Trans. Magn. MAG-22, 1747 (1986).

⁵Thio, Y.C. and Frost, L.S., "Non-Ideal Plasma Behavior of Railgun Arcs," IEEE Trans. Magn. MAG-22, 1757 (1986).

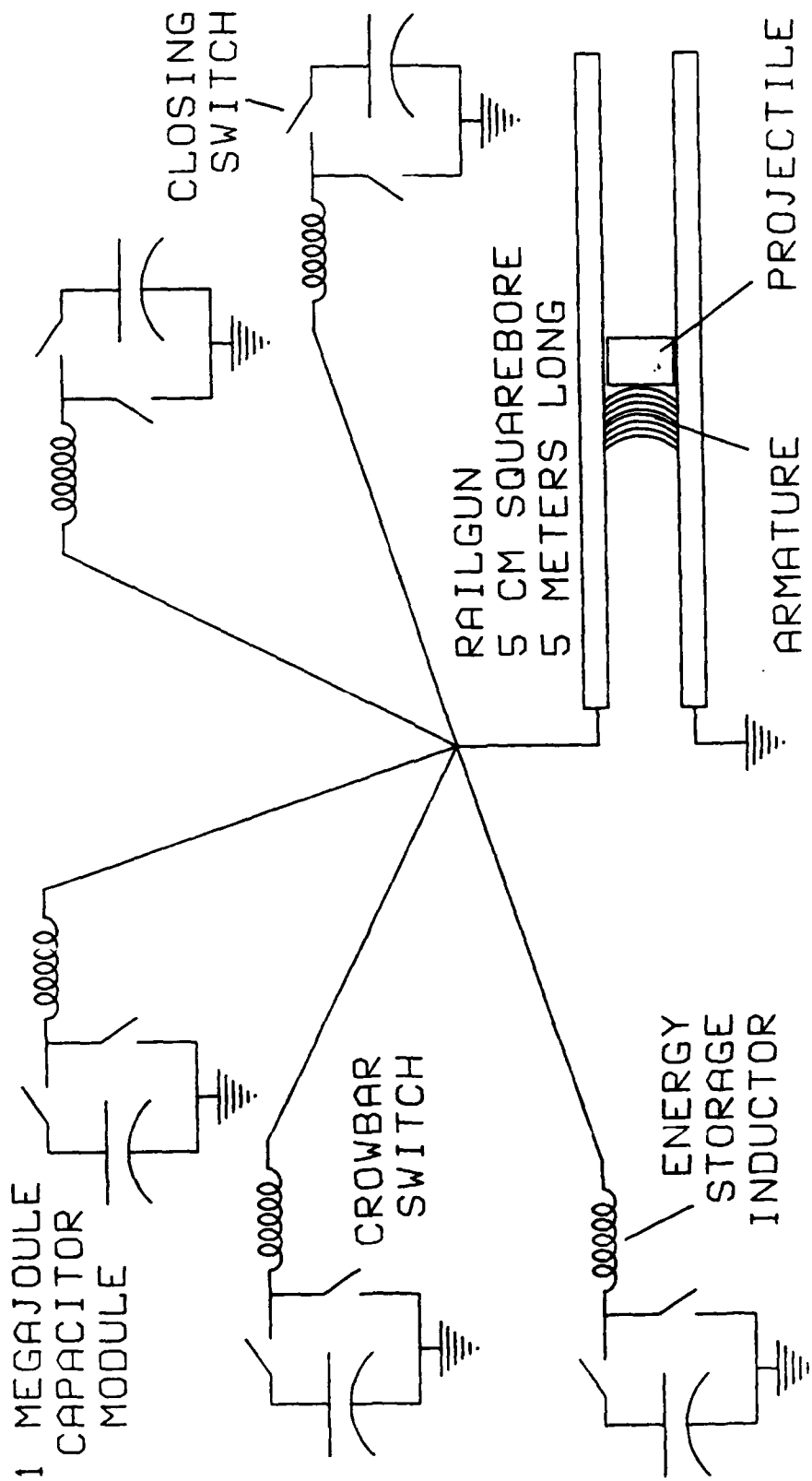


Figure 1. Schematic Illustration of CHECMATE Railgun and Power Supply.

one-dimensional, steady-state model to infer certain properties of the arc which cannot be measured directly. The report is organized as follows. In Sec. II we describe the diagnostic probes constructed especially for these experiments, indicate the specific measurements made, and analyze the data to infer the current density and arc length. In Sec. III, we indicate some revisions undertaken on a model previously developed by Powell and Batteh,² and then use the revised model to calculate properties of the plasma that cannot be measured directly. In Sec. IV are contained our conclusions and recommendations for further study.

II. EXPERIMENTAL RESULTS

1. Diagnostic Probes

The measurement of electrical quantities on a railgun requires particular care to minimize the interactions of its characteristically intense electric and magnetic fields. Probes must be provided with the maximum practicable insulation possible and multiple grounds, establishing loops in which currents may be magnetically induced, must be diligently avoided. All of the diagnostic techniques employed have been previously used and refined on the small BRL railgun.⁶ The voltages produced by the probes were digitally sampled at a preset rate using Nicolet oscilloscopes. These histories were then stored on floppy discs after each firing. The discs were later read into the BRL-LFD VAX 8600 for analysis. Each type of probe and its response characteristics are briefly described in the sections following. The only additional data used in this analysis were railgun current-time histories and the shot-start locations. To obtain the gun's current-time histories, signals⁷ were recorded from calibrated Rogowski loops encircling each of the five power-supply module-output leads. These signals were integrated and summed to give the total current delivered to the railgun.

The conditions and performance parameters of each of the four firings are summarized in Table I. For reference we shall utilize the shot number from the Maxwell firing log.

TABLE I. Description of Shot Parameters

<u>Maxwell Shot#</u>	<u>Projectile Mass</u>	<u>Peak Current</u>	<u>Velocity</u>	<u>Injection Velocity</u>	<u>Capacitor Charge Voltage</u>
94	120 g	1.210 MA	2.37 km/s	680 m/s	35 kV
95	233 g	1.214 MA	1.86 km/s	500 m/s	35 kV
96	120 g	1.215 MA	2.36 km/s	680 m/s	35 kV
97	233 g	1.404 MA	2.105 km/s	500 m/s	39 kV

⁶Jamison, K.A. and Burden, H.S., "A Laboratory Arc Driven Rail Gun," Ballistic Research Laboratory Report No. ARBRL-TR-02502, June 1983.

⁷Wilkinson, G.M. (unpublished data).

a. Voltage Probes

Since very different voltages exist at the two ends of the railgun, the breech and muzzle ends of the rails were each shunted by a resistive chain that was linked through a terminated Pearson current transformer (see Fig. 2); the voltage output of the Pearson was thus proportional to the source voltage. Series diodes isolated the probe circuits from the discharge of CHECMATE's negatively charged sense capacitor on passage of the projectile.

b. B-Dot Loops

In these measurements, the time rate of change of the armature induction field is sensed in a coil oriented to be insensitive to the fields produced by the currents in the rails. Essentially, the coil axis must be parallel to the rail currents and perpendicular to the armature current. When an armature carrying megampere currents, with accompanying 10 to 25 Tesla induction fields, passes a point at speeds of the order of 1 km/s, the rising and falling field intensity can develop a significant induced voltage in even a small conducting loop. The relative orientations and typical output for such a coil are shown schematically in Fig. 3 together with the governing equations for the induced signals. Table II denotes the locations and dimensional details for each of the stations mounted in the CHECMATE barrel for these experiments. With five-turn coils less than one centimeter in diameter, we have measured inductive signatures up to seven volts in amplitude using the probe assembly shown in Fig. 4. This assembly was designed particularly for compactness so that the hole in the sidewall of the CHECMATE barrel needed to accommodate it would cause the least possible weakening of the structure. The modification of the CHECMATE sidewall to accept the probe is shown in Fig. 5. The view of the probe shown in Fig. 4 is rotated 90° with respect to the perspective in Fig. 5.

TABLE II. Probe Stations and Dimensions

	<u>Station 1</u>	<u>Station 2</u>	<u>Station 3</u>	<u>Station 4</u>
Distance from Arc Initiation; Shots 94 and 96	58.4 cm	83.8 cm	109.2 cm	134.6 cm
Distance from Arc Initiation; Shots 95 and 97	68.6 cm	94.0 cm	119.4 cm	144.8 cm
Number of Turns	5	5	5	5
Center of Bore to Loop Center	5.30 cm	5.36 cm	5.33 cm	5.40 cm
Loop Diameter	0.876 cm	0.876 cm	0.876 cm	0.876 cm

*NOTE: The exact location of arc initiation varies with the injection velocity which is different for each projectile mass.

c. Fiber-Optic Light Probes

The plasma armature is, to understate the case, highly luminous. Our experience in routing light from the bore to a reverse biased PIN diode has indicated that, even without drilling completely through the insulating

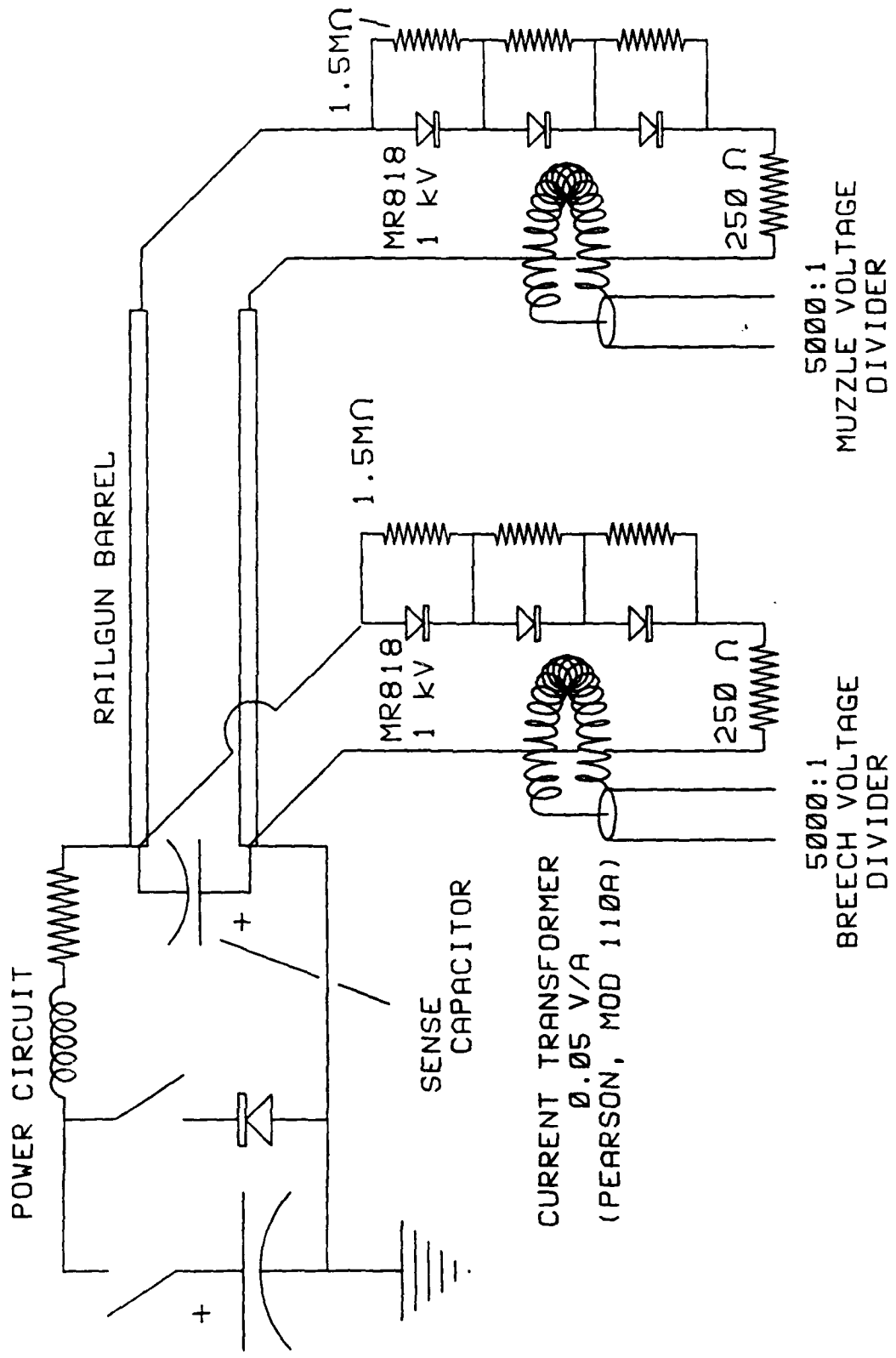
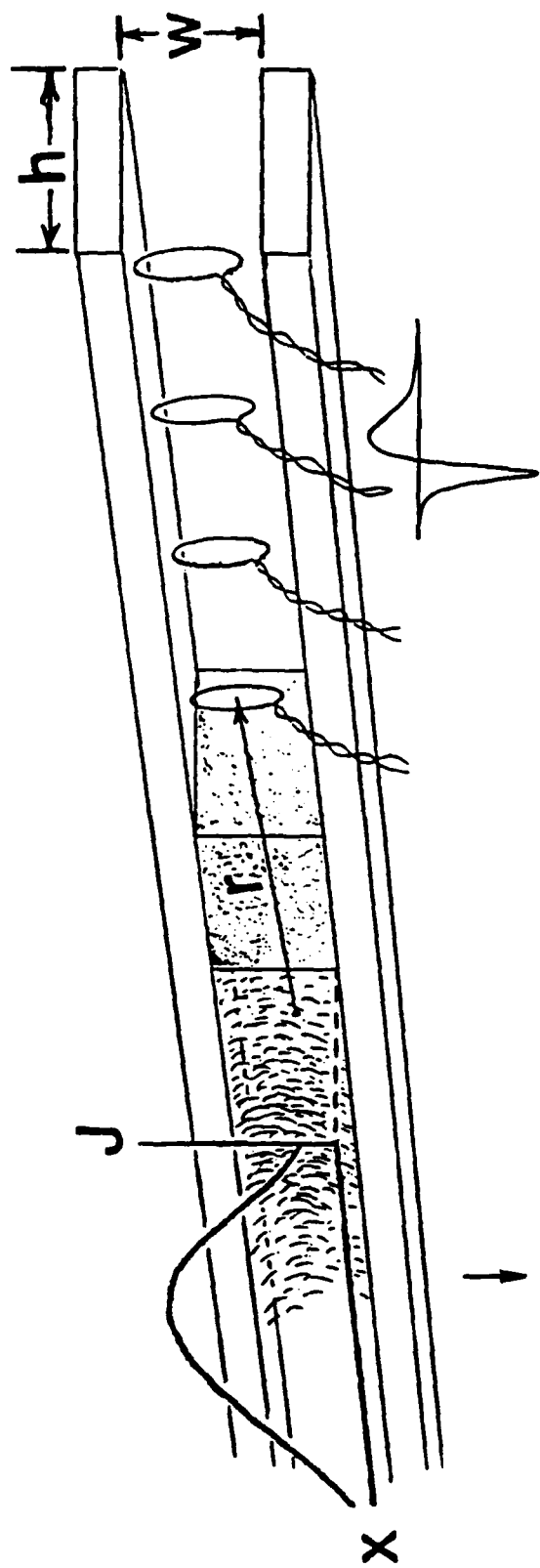


Figure 2. Schematic Circuit for Breech and Muzzle Voltage Probes.



$$\vec{B} = \frac{\mu_0}{4\pi} \int \frac{\vec{J}(x,t) \times \vec{r}_1}{|r^3|} dV \rightarrow \text{Voltage} = -\dot{\vec{B}} \cdot \text{Area}$$

Figure 3. Orientation and Voltage Response of B-Dot Coils.

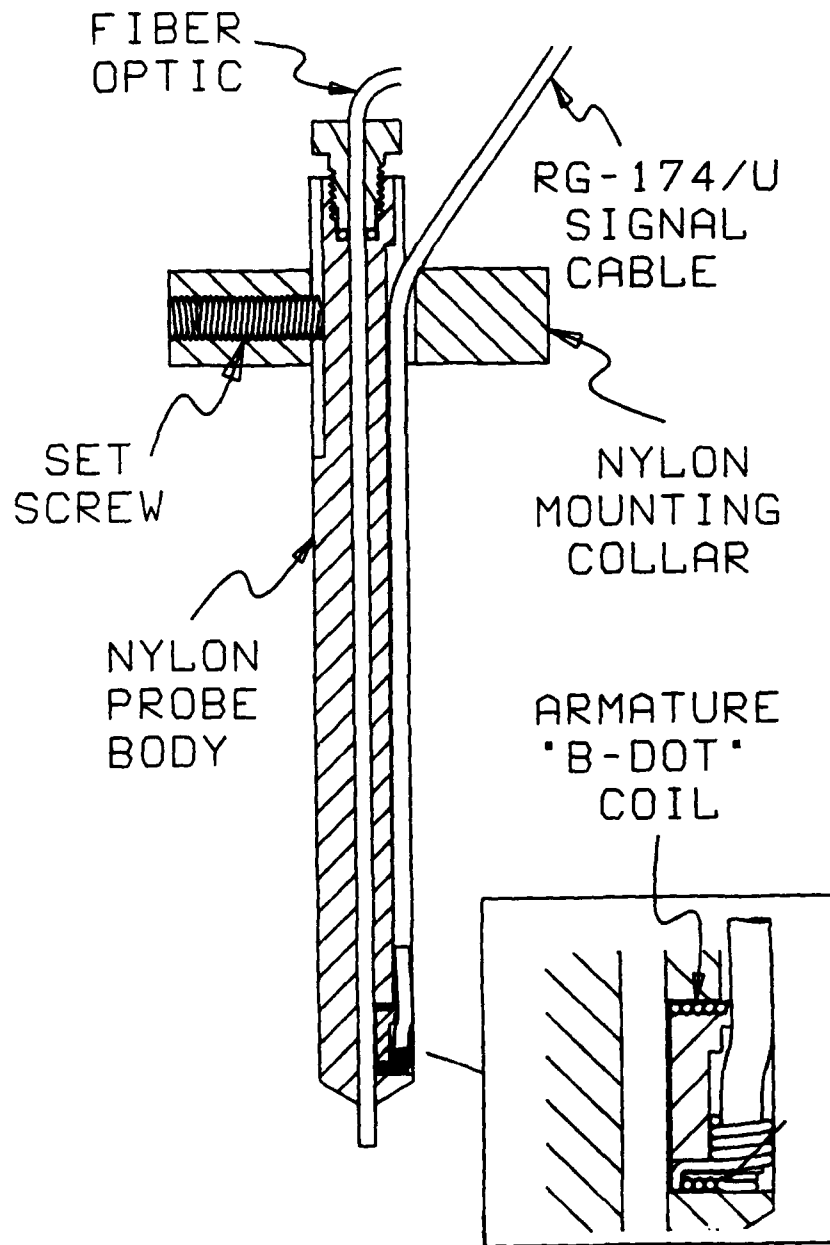


Figure 4. Induction Field and Light Emission Probe Assembly.
A cross section is shown.

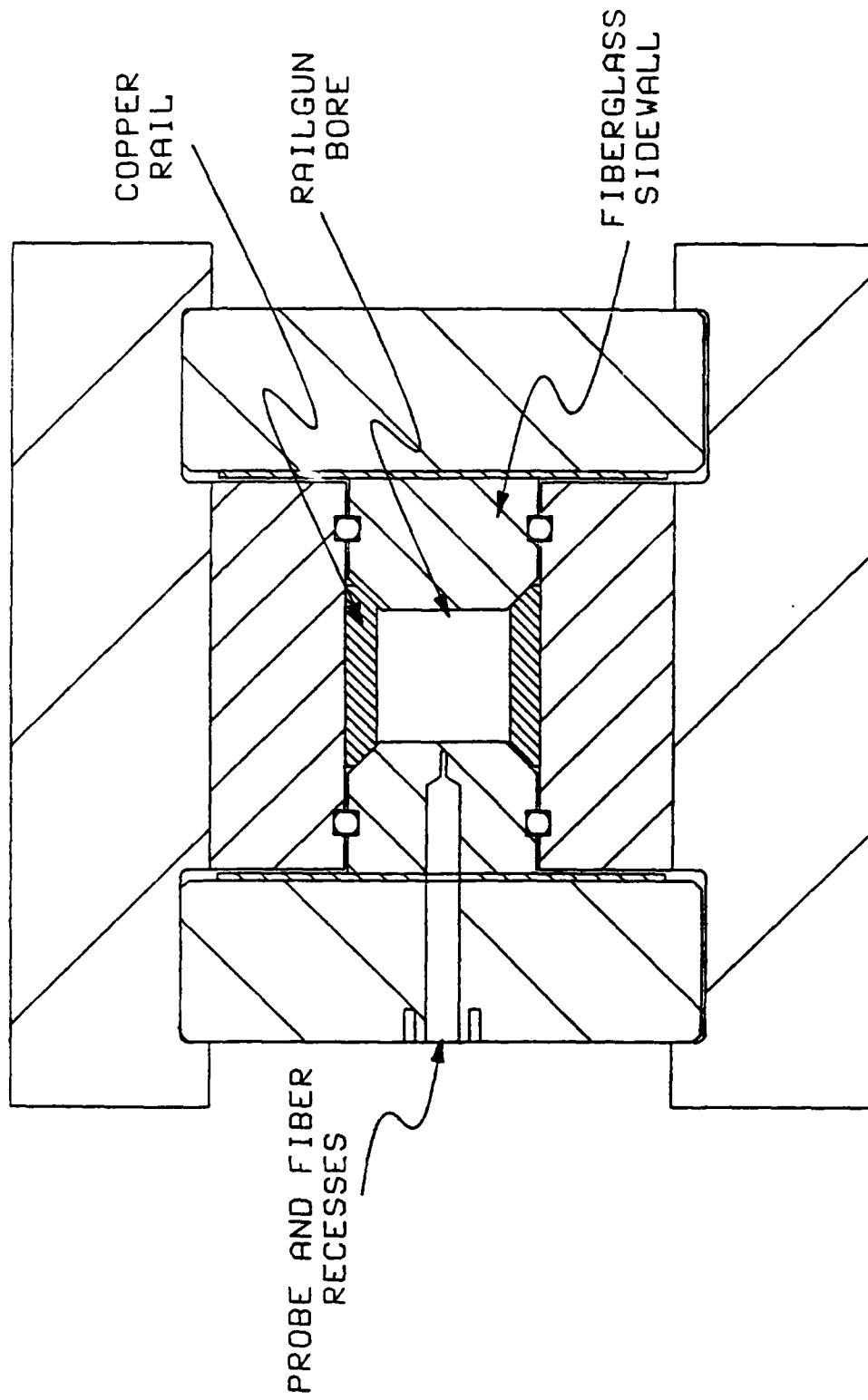


Figure 5. Cross Section View of Probe Mounting Location in CHECMATE Barrel Structure.

sidewalls of the railgun, a satisfactory signal will be generated as the plasma armature passes. Figures 4 and 5 show the method of positioning the fiber optic. The thickness of insulator separating the bottom of the fiber optic cavity and the bore surface was 0.64 cm; the choice of this thickness represents some conservatism over that originally specified.

The fiber optics were routed to a well-shielded box, physically and electrically separated from the gun barrel, and which enclosed the PIN diodes used to sense the light. The remainder of the circuit is shown in Fig. 6. The battery was connected with polarity such that the diode blocked current flow. As the diode is illuminated, however, liberated electrons constitute a current proportional to the incident light flux and the voltage drop across the diode. This current produces a voltage drop in the load resistor nearly proportional to the light intensity. Because the amplitude of this voltage varies over a range limited by the supply voltage, the original 9-volt battery was changed to 67 volts to compensate for the increased cavity wall thickness discussed above.

2. Measured Quantities

The probes described in the previous section were utilized to measure the following quantities:

- o Rail (armature) current
- o Breech voltage
- o Muzzle voltage
- o Time derivatives of the armature induction field
- o Light emission to the insulating portion of the barrel
- o Armature location versus time.

a. Current

Figure 7 is a representation of the current-versus-time plots measured by integrating and summing the Maxwell Rogowski coil signals from each of the five capacitor banks. The waveform is typical of a crowbarred inductor circuit which is characterized by a rapid rise to peak current followed by a nearly exponential decay. Current waveforms from Shots 94 and 96 are nearly identical and are indistinguishable in Fig. 7. Table I above lists for each of the four shots a value of peak current. In practice, for the times when the armature is near the probe array, the current may be accurately modeled by

$$I(t) = I(0) \exp (-t/\tau) \quad . \quad (1)$$

This equation allows two quantities, $I(0)$ and τ , to be used in the computation of the instantaneous current at times when the armature is close to the probe array. Table III, in Sec. e below, gives values for both the scaling constant and the decay constant which describe the railgun current for all four shots.

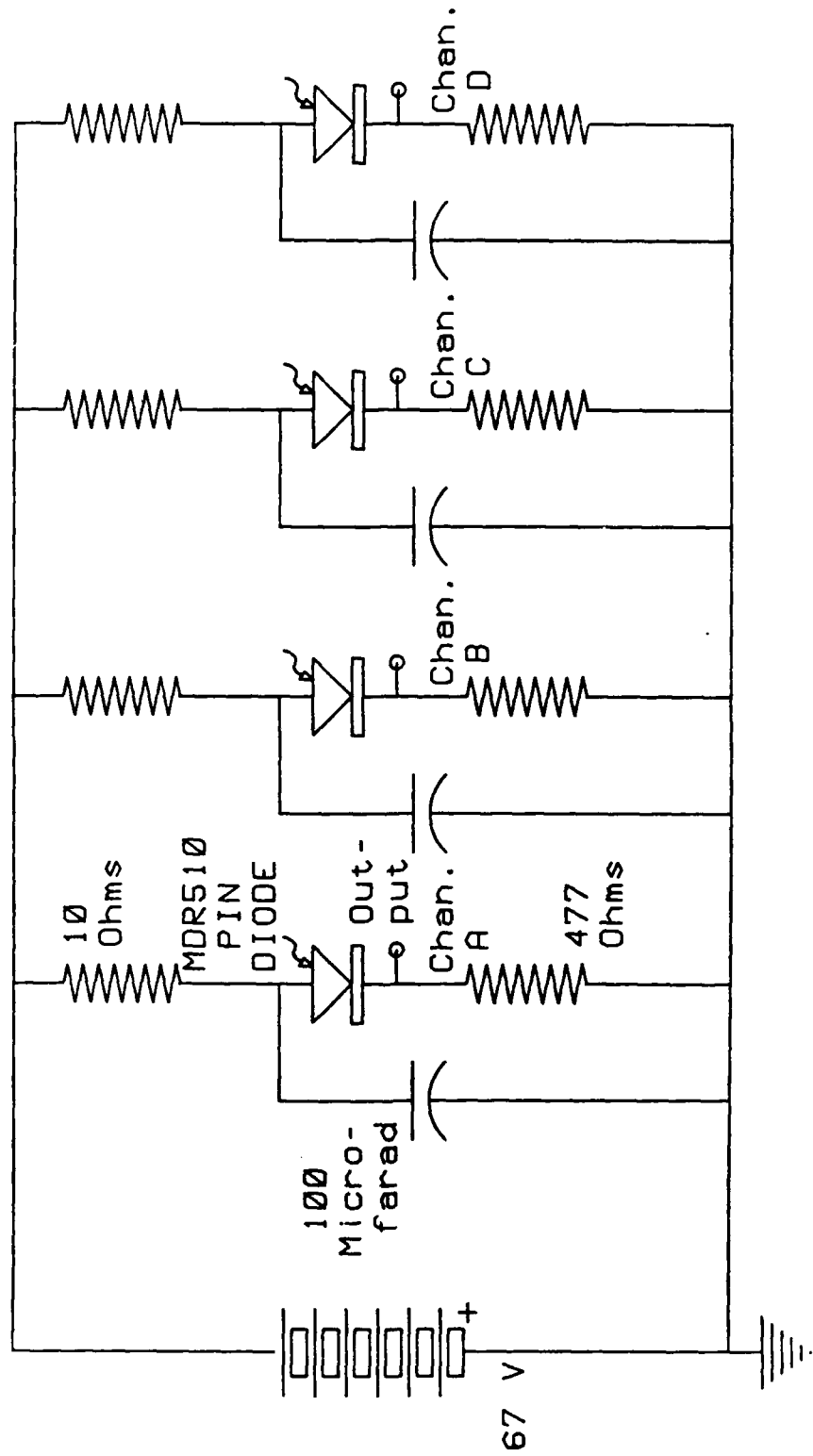


Figure 6. Schematic Circuit of PIN Diode Light Detectors.

Shot 94
Shot 95
Shot 96
Shot 97

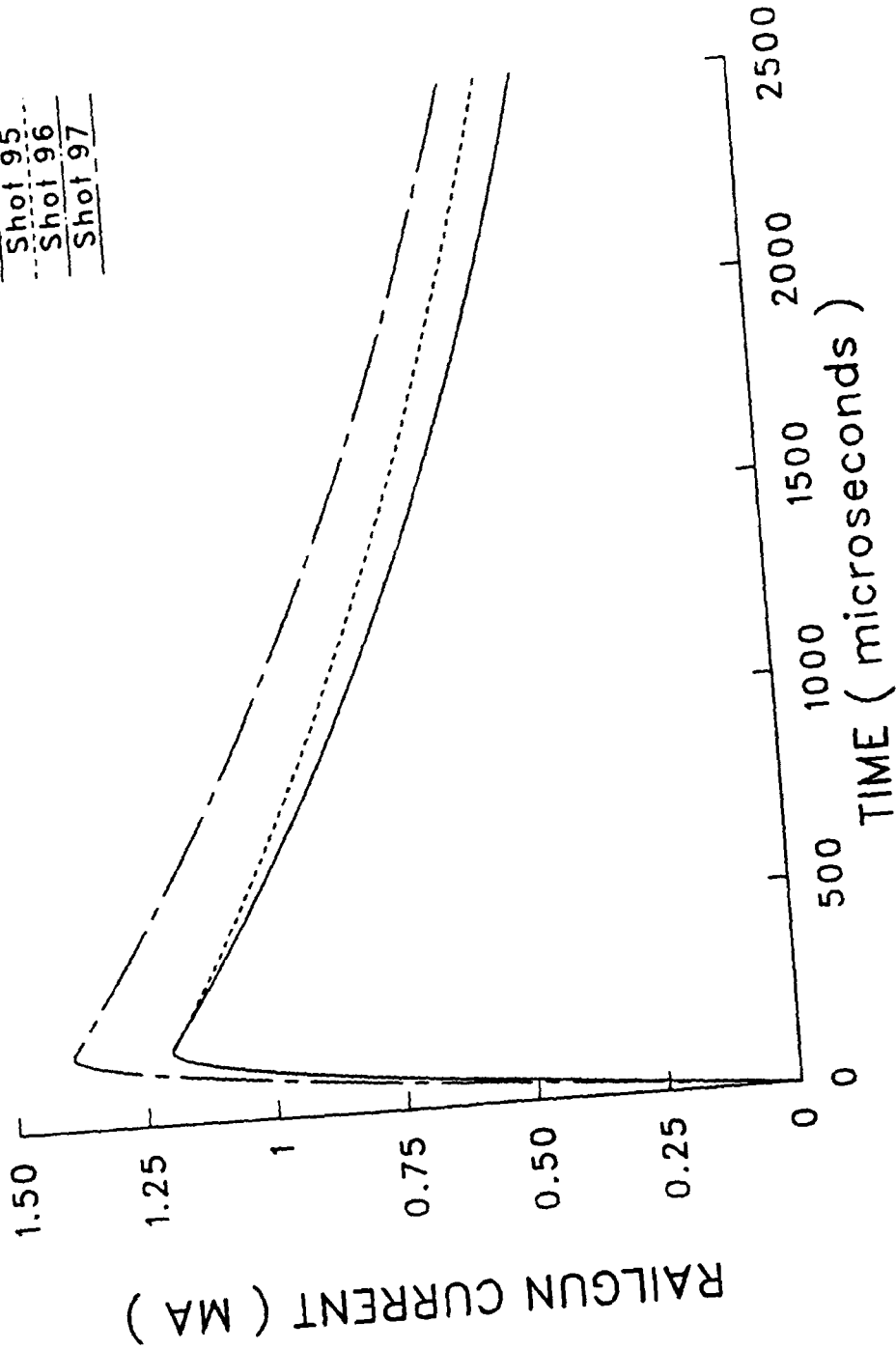


Figure 7. Railgun Current Versus Time Waveforms for Shots 94-97.
The profiles for Shots 94 and 96 were coincident.

b. Breech and Muzzle Voltage

The voltage across the extreme tip of the arc drives the current sensed in the muzzle voltage circuit. This circuit contains only portions of the rails in which no propulsive current is flowing so self-inductive and resistive effects of these large currents are not superimposed on the measurement. (Mutual inductance between the propulsive and the measuring circuits may also be shown to be very small.) The voltage seen is, then, the resistive voltage across the leading edge of the arc. The breech measurement path, on the other hand, includes both current carrying rails and the trailing edge of the armature. This path surrounds a growing volume of flux driving the armature. The resulting inductive voltages are, thus, added to the resistive voltage developed across the rear portion of the armature. Figure 8 shows breech and muzzle voltage traces for Shots 96 and 97. The rapid fall of both voltage traces during the early portion of the shot, 0 to 300 microseconds, signals the formation of the armature plasma. After 500 microseconds the voltage drop becomes relatively constant at or near 300 V. The muzzle voltage of only 300 V is lower than anticipated for a 5 cm bore railgun. Of particular interest are the muzzle voltage jumps at 2.4 ms and 2.9 ms for Shots 96 and 97, respectively. These jumps are characteristic of the armature exit from the railgun when there is still sizable field energy in the inductor and between the rails. We also note the lack of such jumps in the breech voltage suggesting that the armature was quite long near the end of the shot.

c. Armature Induction Field

The armature induction field, B , is not directly sensed; instead, its time derivative, "B-dot," is measured at four locations. This measurement constitutes the standard against which a modeled counterpart is compared as a test of the success in the modeling procedure developed to unfold the armature current density. The characteristic form of a B-dot trace is a relatively sharp negative peak followed by a wider, lower amplitude positive peak. The polarity of these peaks is tied to the chosen orientation of the B-dot coil. As the distributed current in the arc approaches the array of coils, each of its elements is contributing to each respective fall in voltages sensed. As the midpoint of the distribution passes a given coil, the effect of the portion of the current which has already passed and is receding matches the effect of the portion still to come and the response passes through zero. Finally, as the bulk of the current is receding down bore, the polarity reverses.

Figures 9 through 12 show the B-dot traces for each of the four stations for Shots 94 through 97. The individual points are the digitized voltages induced in the loops imbedded in the barrel and smooth lines are those calculated by the fitting procedure to be discussed in the next section. The random point-to-point variations are apparently real and the disturbances superimposed on the later portions of the traces may be caused by small arcs behind the original one. The nearly equal amplitudes from the different probes suggest that the increasing length of the arc and the decay of the total current which reduce the B-dot signals are nearly balanced by the increase in velocity which boosts the B-dot signals.

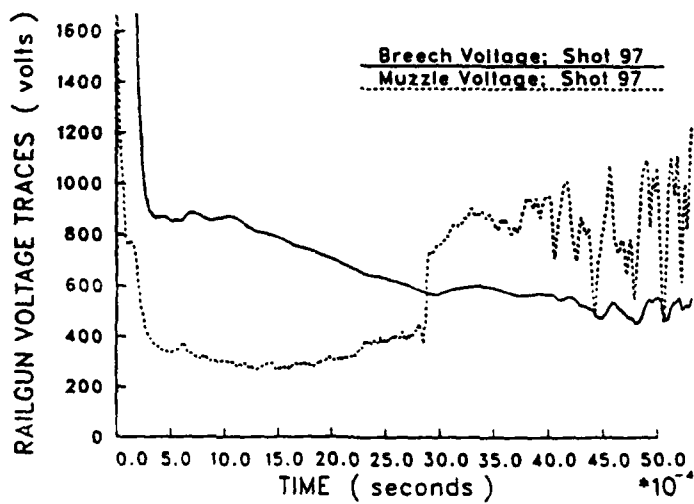
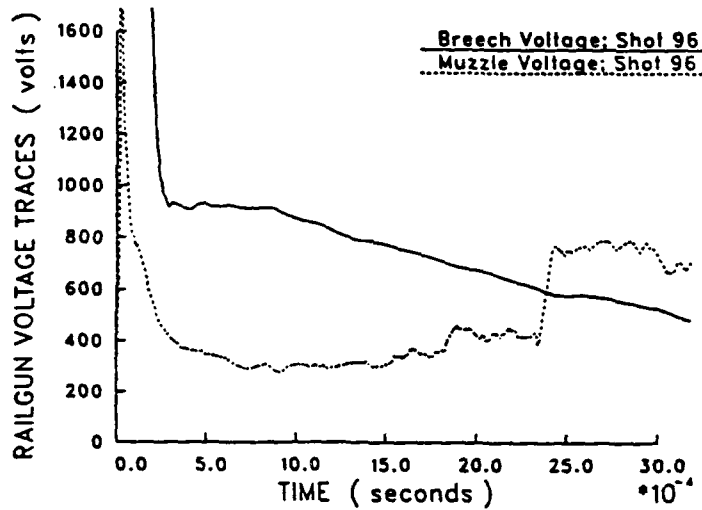
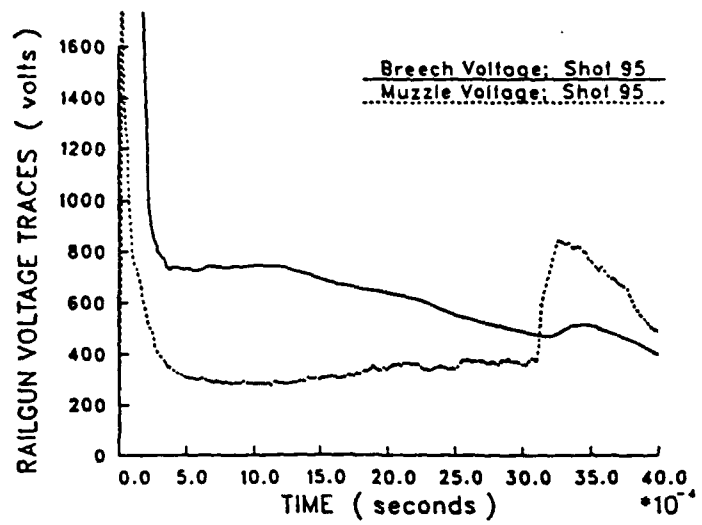


Figure 8. Breech and Muzzle Voltage Traces for Shots 95, 96 and 97.

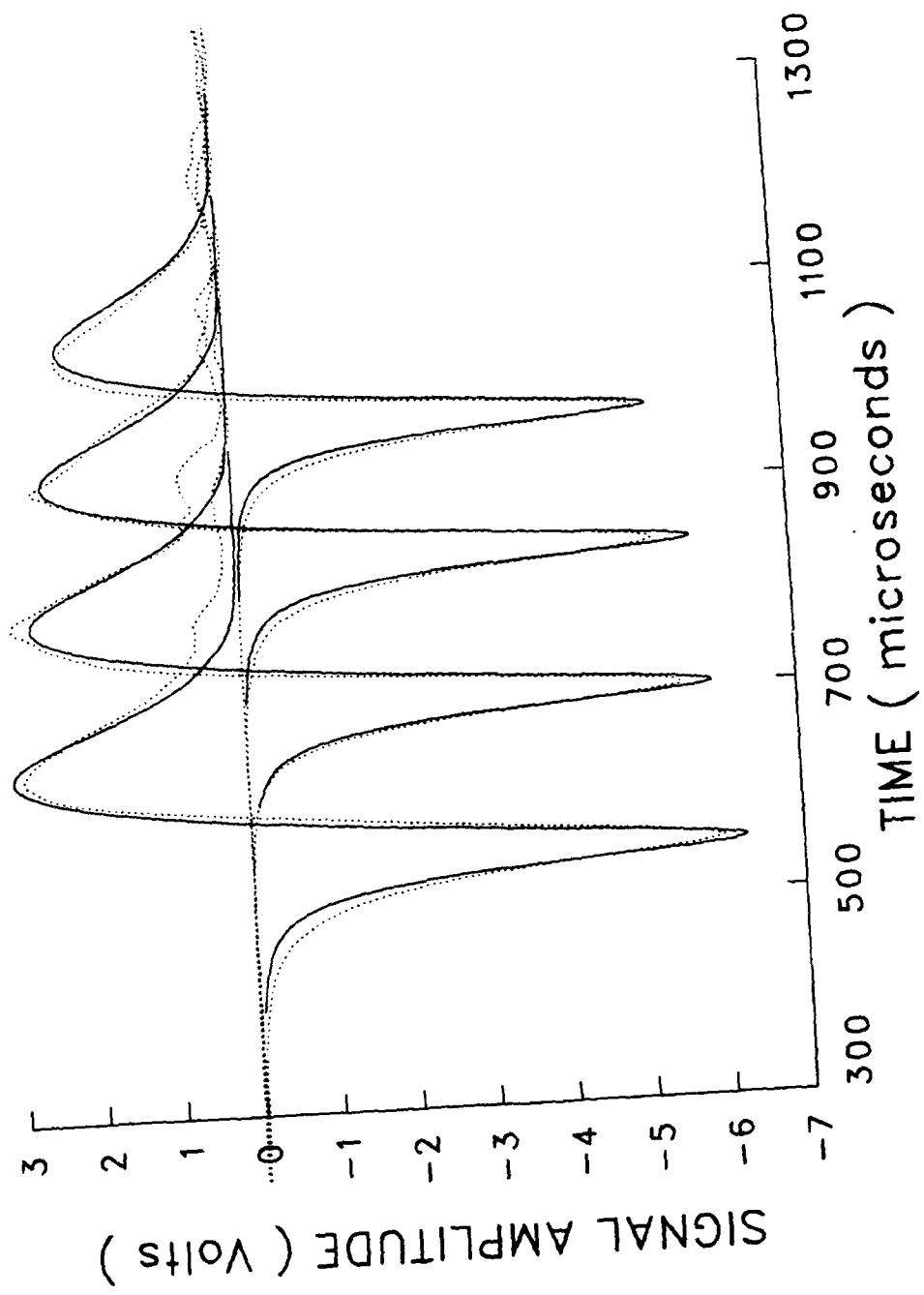


Figure 9. Four Station B-Dot Loop Voltage Signals; Shot 94.

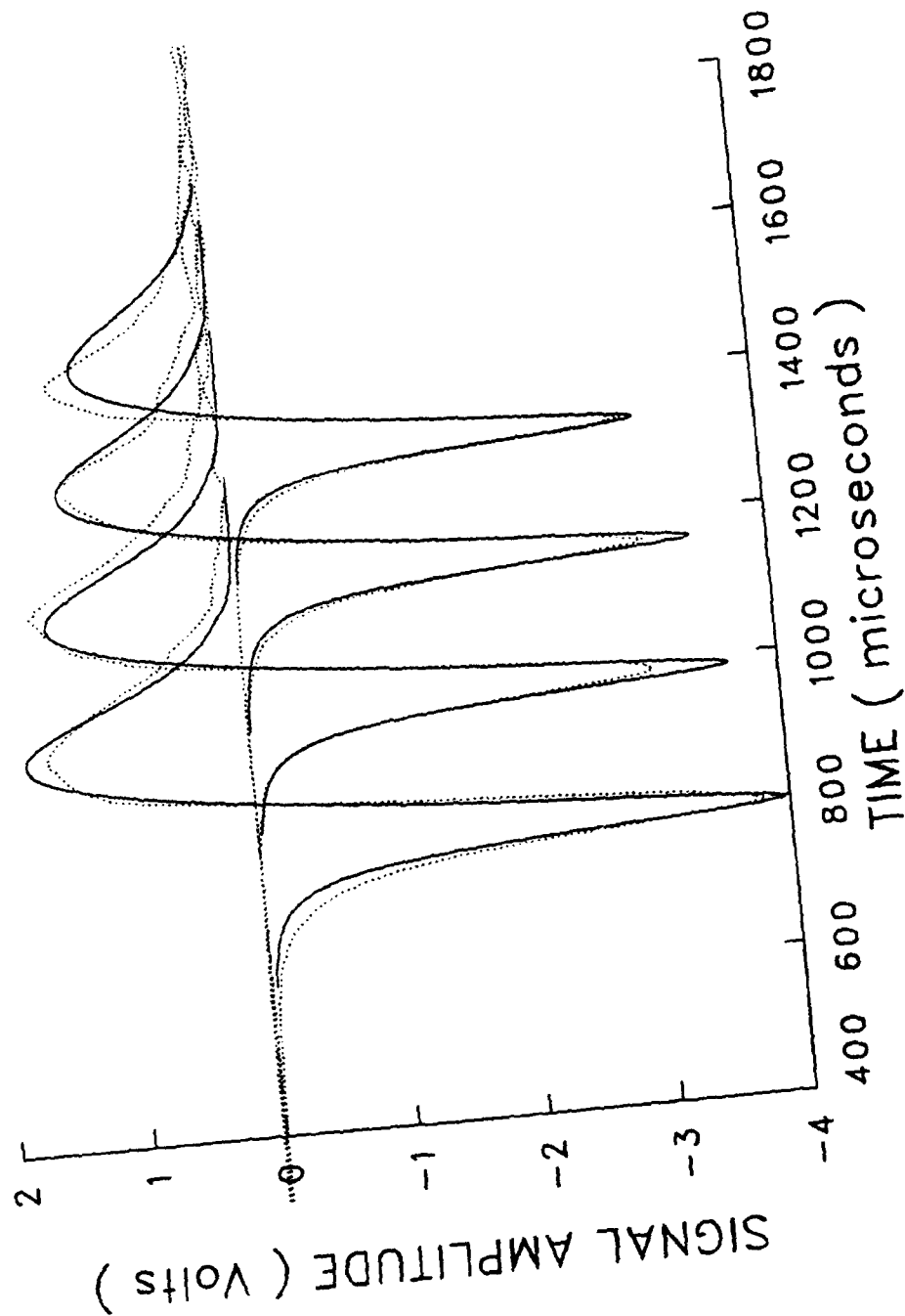


Figure 10. Four Station B-Dot Loop Voltage Signals; Shot 95.

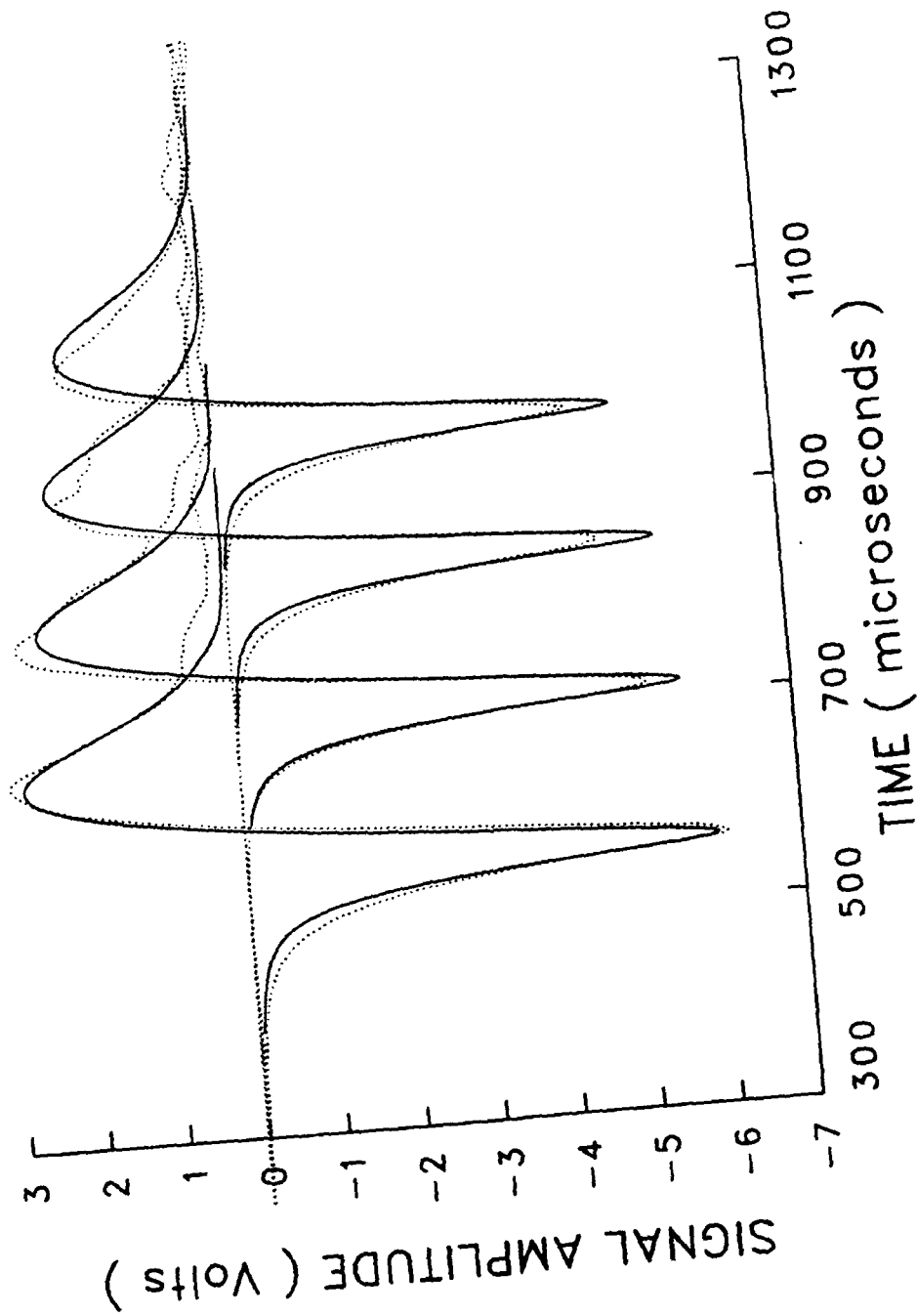


Figure 11. Four Station B-Dot Loop Voltage Signals; Shot 96.

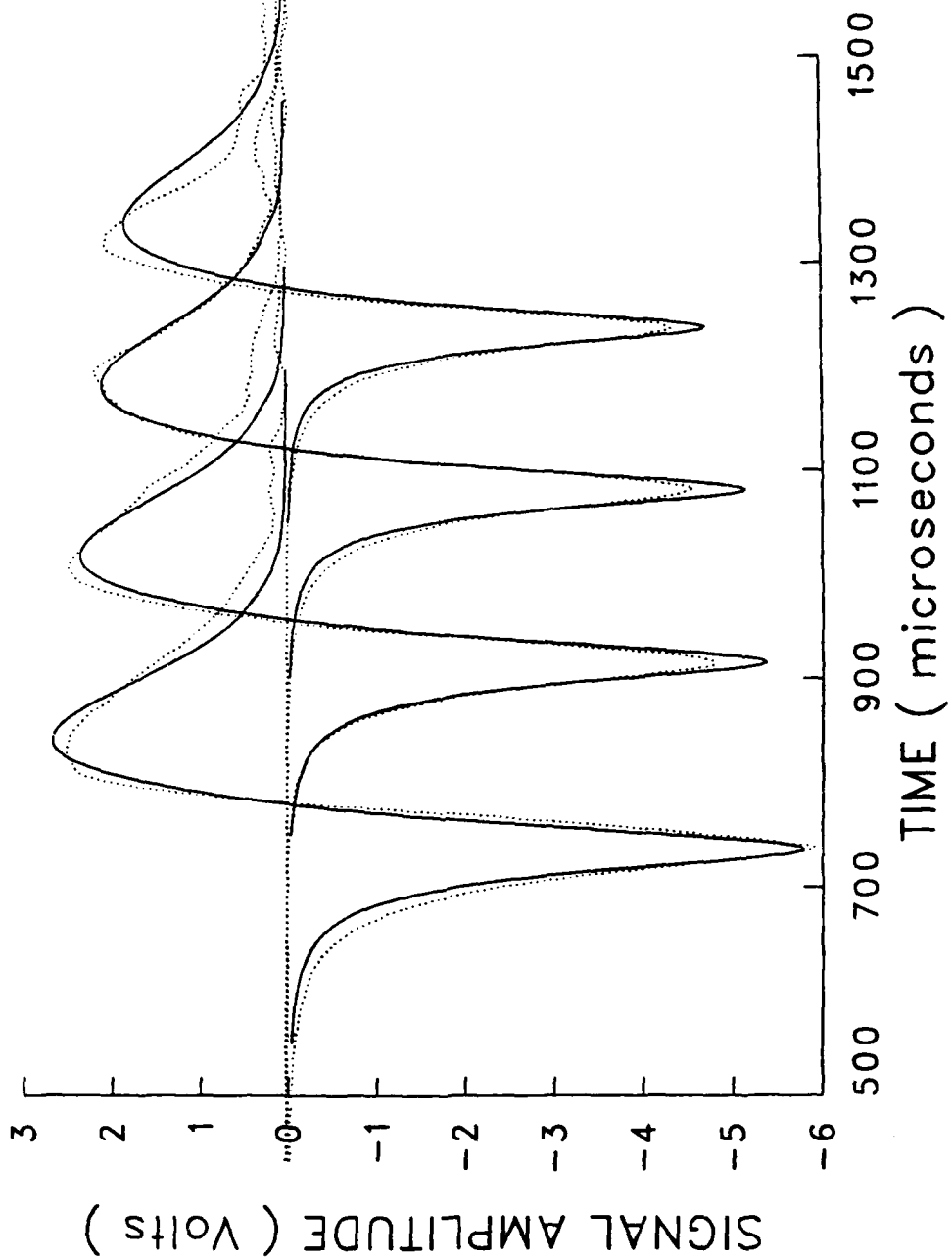


Figure 12. Four Station B-Dot Loop Voltage Signals; Shot 97.

d. Light Emission

The observed intensity of emitted light as a function of time at each of the four probe stations is plotted for Shots 95 and 96 in Figs. 13 and 14. The differences in vertical scale maxima are an indication of the variation in sensitivity of the uncalibrated PIN diodes, and should not be used to infer relative intensities among stations. For Shot 95, the initial sharp rise in light intensity indicates passage of the armature-projectile interface; for Shot 96, however, luminosity ahead of the sharp rise indicates leakage of luminous material past the projectile into the bore ahead of it, from 500 to 700 microseconds at probe station 2. The extended leakage path and greater stability of the longer, heavier projectile used in Shot 95 offer an explanation of this observation. On Shot 94 our digitizing instrument was set on too sensitive a scale and the signals saturated the amplifiers. On Shot 97 the recording equipment failed to record all but one of the light emission signals.

e. Armature Location Versus Time

Our method of analysis of armature current density from B-dot signatures requires knowledge of the location of the leading edge of the arc versus time. Normally, we would use the sharp rise in the fiber optic data to determine the position-versus-time function; however, the loss of some fiber optic data and the uncertainty introduced by the precursor luminosity described above, have led us to use the time of the first negative peak of each of the four B-dot stations to determine the coefficients of the cubic equation

$$X_p(t) = A_1 t^3 + A_2 t^2 + A_3 t + A_4 \quad (2)$$

Here $X_p(t)$ denotes the position of the projectile-armature interface. From this information (see Table III), the acceleration may be derived and plots of acceleration versus time are shown in Figs. 15 and 16. The accuracy of this method is probably only on the order of 10 percent, but it is good enough to show that the ideal accelerations, predicted from the effect of the calculated armature forces on the projectile mass, are too high. Bore friction and energy required to drive a shock ahead of the projectile could account for most of this discrepancy.

TABLE III. Shot Parameters Used in Data Analysis

	<u>Shot 94</u>	<u>Shot 95</u>	<u>Shot 96</u>	<u>Shot 97</u>
I(0)	1.30 Ma	1.28 Ma	1.30 Ma	1.49 Ma
τ	2.17 ms	2.55 ms	2.17 ms	2.50 ms
A_1	-1.1802×10^8	-4.9575×10^7	-7.254×10^7	-3.4926×10^7
A_2	7.0107×10^5	3.9912×10^5	6.5462×10^5	4.1452×10^5
A_3	944.27	757.80	938.40	801.34
A_4	-0.12780	-0.14770	-0.13405	-0.11603

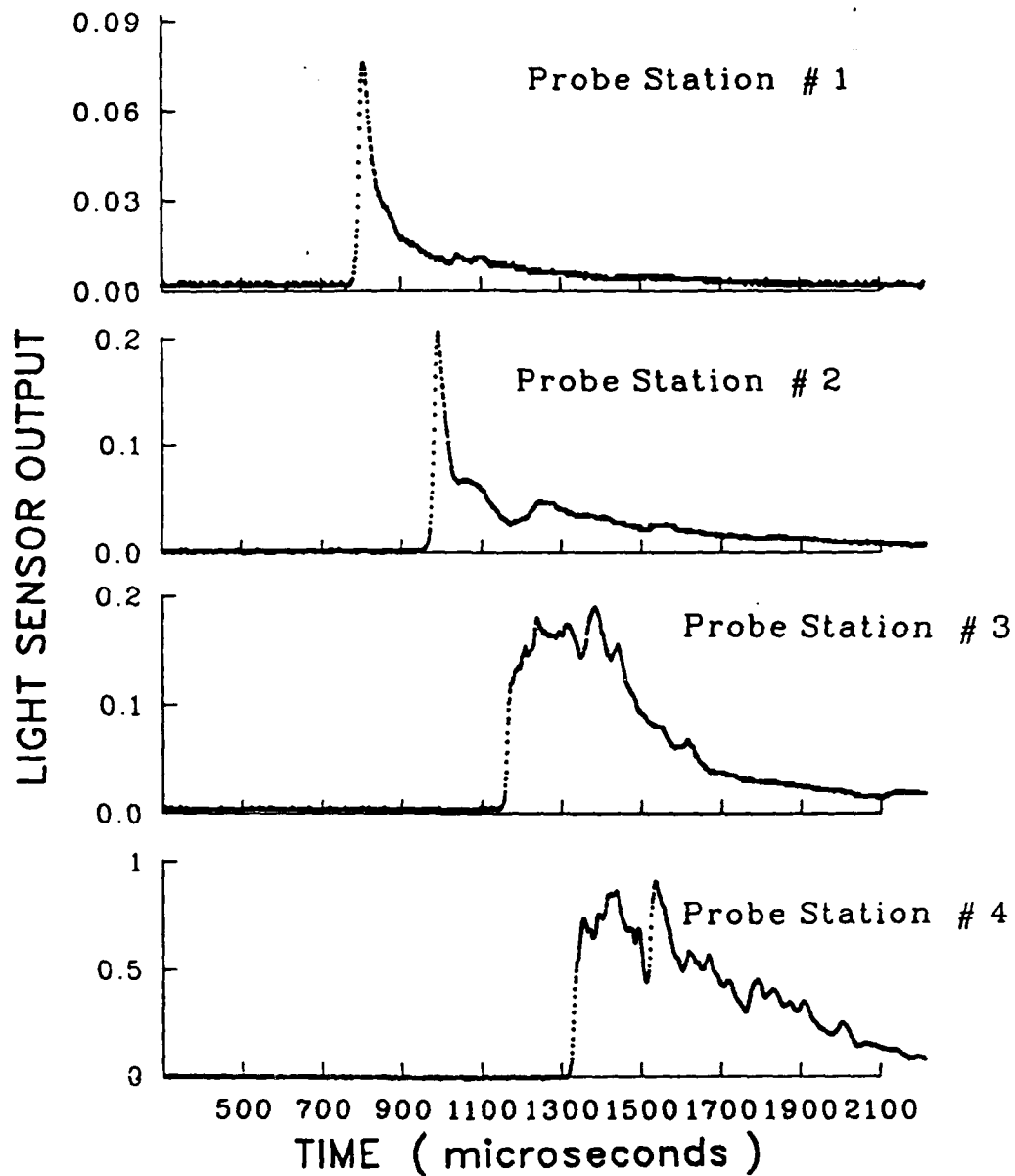


Figure 13. Light Intensity Versus Time Traces from Four Probes; Shot 95.

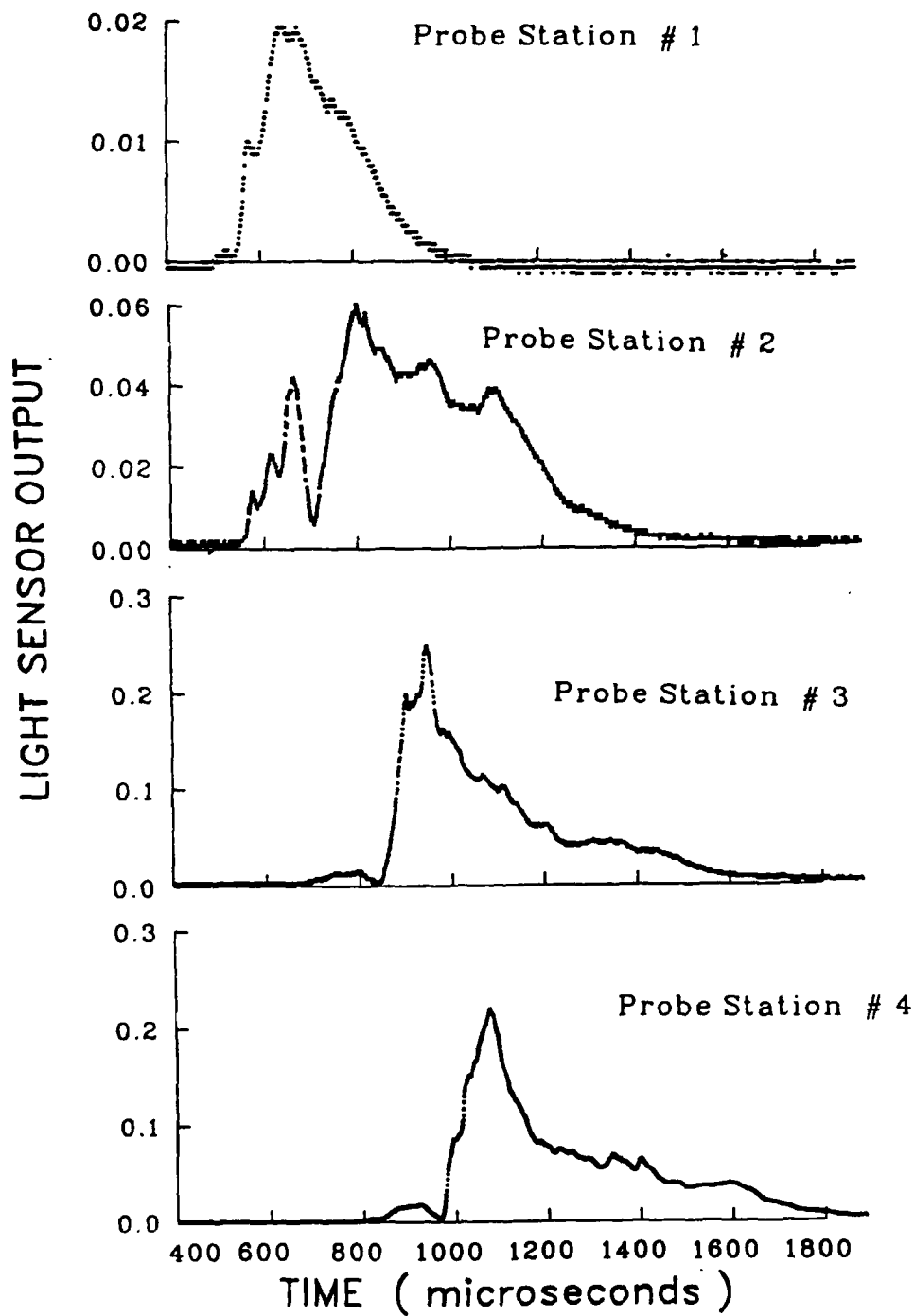


Figure 14. Light Intensity Versus Time Traces from Four Probes; Shot 96.

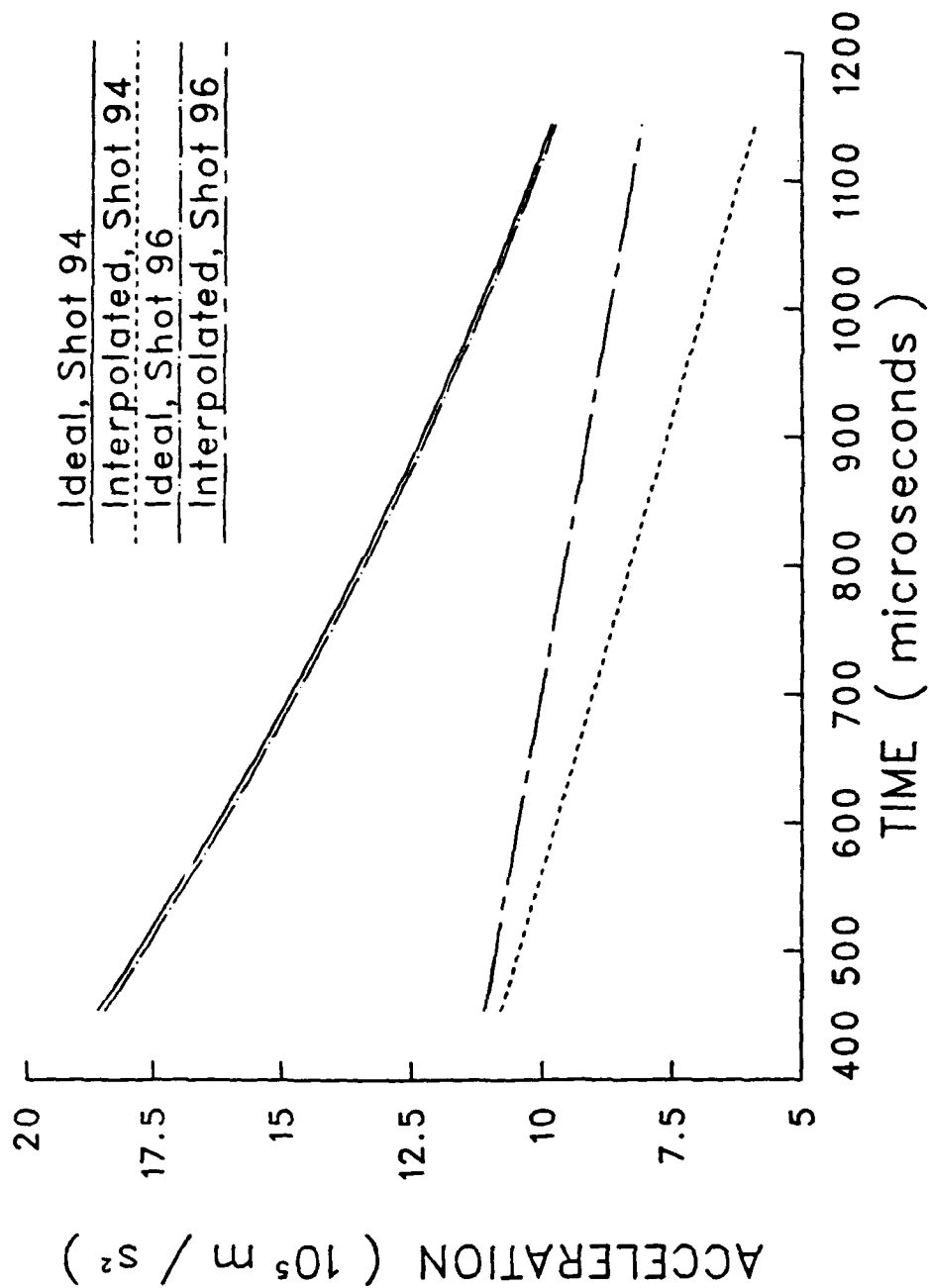


Figure 15. Ideal and Interpolated Accelerations for CHECMATE Railgun Shots 94 and 96.
The projectile mass was 120 g.

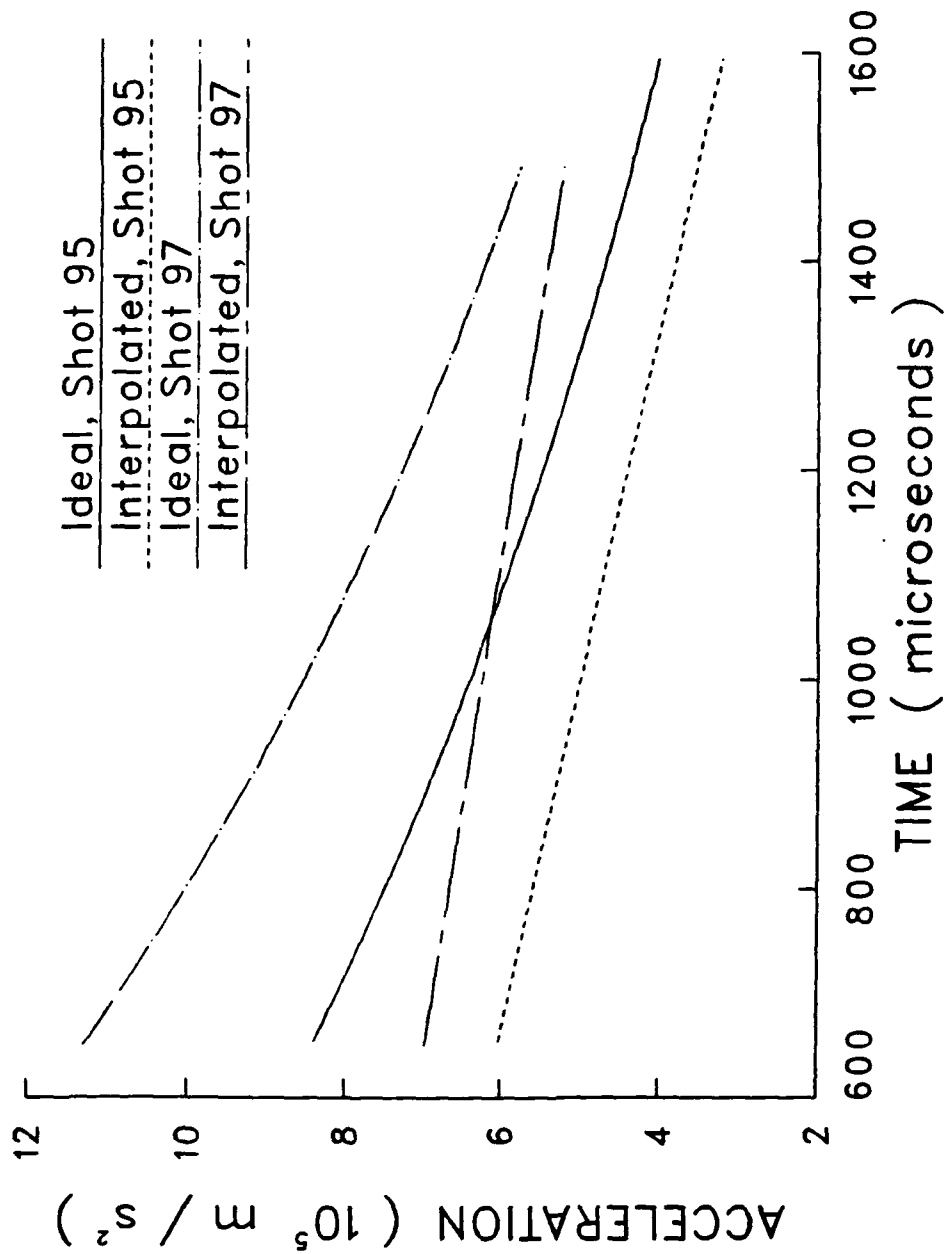


Figure 16. Ideal and Interpolated Accelerations for CHECMATE Railgun Shots 95 and 97.
The projectile mass was 233 g.

3. Data Analysis

a. Current Density from B-Dot Signatures

A source of further understanding of the plasma armature properties may be found by setting the time derivative of the Biot-Savart integral (Fig. 3) equal to instantaneous values of the field derivative sensed by a B-dot coil. Then, an unfolding operation may reveal the kernel of the integral $J(x,t)$ which is the distribution of current within the armature. Because there is no reason to believe that only one distribution of current is capable of producing the observed field distribution, not enough information is available to allow a unique analytic solution to this problem. In our previous work,⁸ however, we have developed a computer technique for modeling a moving, current distribution and the effect of its magnetic field on a stationary B-dot coil. We artificially provide added information by using a modification of the Gaussian curve function, truncated at the plasma-projectile interface (see Fig. 17):

$$J(x,t) = (I_0/c_n) \exp [-(x-X_0)^2/2w^2]$$

where $X_0 = X_p - X(t)$. Figure 17 and Eqs. (3) - (5) define the five adjustable parameters, P_i .

The procedure systematically varies the parameters until the calculated coil response closely fits the B-dot signatures we have measured; in this sense, the distribution is "unfolded" from the B-dot signature.

We have attempted the modeling procedure with a number of different functions but were most successful in matching the set of B-dot traces when using a truncated Gaussian curve function. This Gaussian (or statistical normal) representation of the current-density distribution was chosen for several reasons: First, it contains several parameters whose variation manipulates it to the desired shape. Second, the shape is qualitatively similar to standard theoretically derived profiles.² Third, the formality for normalizing the area is well known and easily usable. The latter requirement is in accordance with the practical necessity that the area (i.e., the integral of the current density over the distribution) should be normalized to the value of the instantaneous, total current. This current is computed using the values of τ and $I(0)$ (an adjusted initial current value) and the given value of time. The value for $I(0)$ is fitting parameter P_5 and is adjusted to improve the fit. The value for τ is fixed at the experimentally measured quantity. A series of calculations, each at a new position as determined from the digitizer time step and Eq. (2), describing this moving distribution's magnetic field, were made using a Biot-Savart volume integral. The time derivative, B-dot, at the position of a given coil was then calculated. With each trial set of parameters, a test of the fit between the calculated B-dot and that seen by the coil was made. The process then directed appropriate changes in the parameters and was repeated iteratively until no further improvement in goodness of fit could be obtained.

⁸Jamison, K.A., Marquez-Reines, M. and Burden, H.S., "Measurements of the Spatial Distributions of Current in a Rail Gun Arc Armature," IEEE Trans. Magn. MAG-20, 403 (1984).

The parameters used to describe the current-density distributions which fit the data best are listed in Table IV. Referring to Fig. 17, we see that $X(t)$, the distance between the peak of the Gaussian and the front truncation point representing the back of the projectile is given by

$$X(t) = P_2 \left(\frac{I(0)}{I(t)} \right)^{P_4} = P_2 e^{P_4 t / \tau} \quad (3)$$

TABLE IV. Current Density Parameters for Acceptable B-Dot Fit

	<u>Shot 94</u>	<u>Shot 95</u>	<u>Shot 96</u>	<u>Shot 97</u>
P_1	0.06924	0.07375	0.06800	0.06646
P_2	0.03701	0.04986	0.03945	0.03699
P_3	1.0717	1.1104	1.2726	1.1527
P_4	-0.0902	0.5518	0.00186	0.4706
P_5	1.374×10^6	1.430×10^6	1.377×10^6	1.66×10^6

where P_4 expresses the power of the current ratio which modulates P_2 , the zero time value of X . The second equality was derived from the first by substitution of Eq. (1).

The characteristic width of the Gaussian is given by

$$W(t) = P_1 \left(\frac{I(0)}{I(t)} \right)^{P_3} = P_1 e^{P_3 t / \tau} \quad (4)$$

where P_3 again expresses a power of the current ratio, this time modulating P_1 , the initial Gaussian width. (W is analogous to the variance of the normal distribution.)

P_5 is the calculated, zero-time value for the decaying current wave form. Though not a measured quantity, it does permit use of an analytic formulation which gives current

$$I(t) = P_5 \exp(-t/\tau), \quad (5)$$

accurately representing the measured current when the armature is near the probes.

P_2 and P_1 are continuously modulated by the factors defined. This representation was chosen primarily to allow comparison between experiment and models whose arc length varies as a power of the inverse of the ratio, instantaneous current to peak current. Note that $X_p(t)$ is given by Eq. (1). The values for τ were not used as fitting parameters, but were taken directly from the data. In this way the time dependence of the current was forced to match the experimental conditions.

After numerous iterations of the five parameters listed above, minimizing the differences between the measured and calculated B-dot signals, we

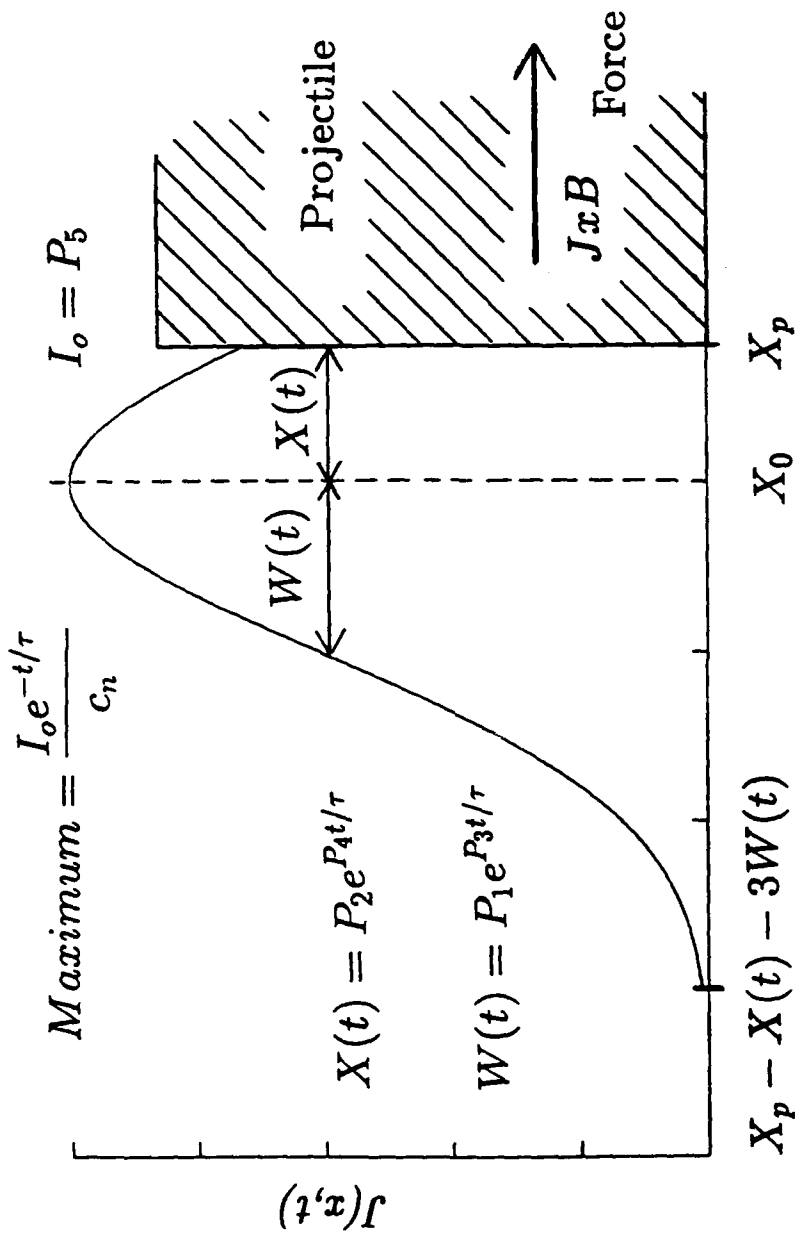


Figure 17. Parametric Description of Armature Current Density Function.

observed the parameters shown in Table IV. All of the parameters except P_4 were very sensitive to the fitting procedure. Since P_2 is not a large number, it is evident that its modulator, P_4 , would not be a critical parameter in determining the calculated B-dot signal. The Gaussian width, P_1 , and its modulator, P_2 , were sensitive fitting parameters and their values for all shots are quite similar.

The parameters above, together with the position-versus-time equation, completely define J for all points in space at all times. The results can be expected to describe J accurately only in the regions of time when some signal is present on the B-dot probes. Because J is a function of two variables, we are able to display the current density in two different ways. The current density J may be plotted either as a function of position at a fixed time or as a function of time at a fixed position. The former is the so-called snapshot view of the armature current; the latter is representative of the armature "flying by" a point on the barrel. Figure 18 graphically displays the spatial distribution of J for four different times during Shot 96. The times have been arbitrarily chosen to correspond to 100 kA intervals as the current decays and the projectile is accelerated down the bore. It is evident from these curves that the arc length is between 20 and 40 cm. Therefore, the peak current density does not exceed 150 MA per square meter.

b. Arc Length

Since the arc length is not defined for a Gaussian function, we have arbitrarily chosen to define the length as the distance from the rear of the projectile to a point in space at which the current density has fallen to one tenth its peak value. For computational purposes, we actually include J where it was larger than one percent of the maximum. This corresponds to a point three Gaussian widths, $W(t)$, behind the maximum value. Figure 19 displays the "arc length," calculated in this manner, versus total current in the armature for each of the four shots. While the cutoff point of our distribution is arbitrary, the trends in time and current variation are real. We see from this plot that the armature length scales nearly as the inverse of the current.

c. Comparison of Current Density and Light Intensity

Figures 20 and 21 show plots of the current density, $J(t)$ versus time for the fixed locations of each of the probes. We have also arbitrarily scaled the light intensity measurements to the peak value of J as it flies by each probe location and plotted it for comparison. It is evident that luminous material not only outruns the projectile in Shot 96 but also lags behind the current carrying portion of the armature in both shots.

Fine structure in the light output is also evident in both shots, particularly at later times. This type of structure was previously observed in data taken from the BRL railgun and can possibly be explained by the existence of Raleigh-Taylor instabilities in the arc.⁹

⁹Powell, John D., "Interchange Instability in Railgun Arcs," Phys. Rev. A, 34, 3262 (1986). See also Ballistic Research Laboratory Report No. BRL-TR-2776, January 1987.

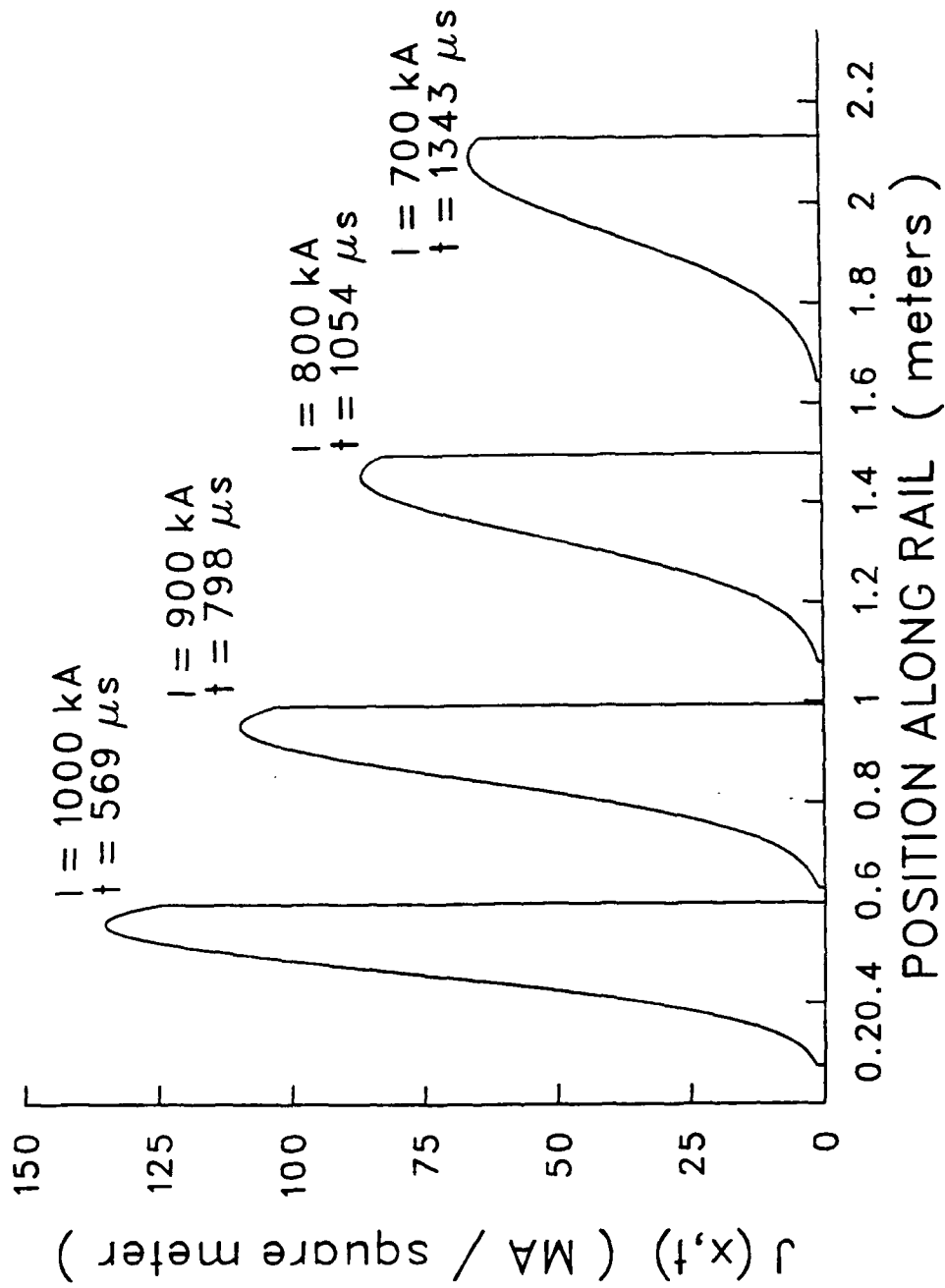


Figure 18. Sample Distribution of the Arc Current Density at Four Different Times; Shot 96.

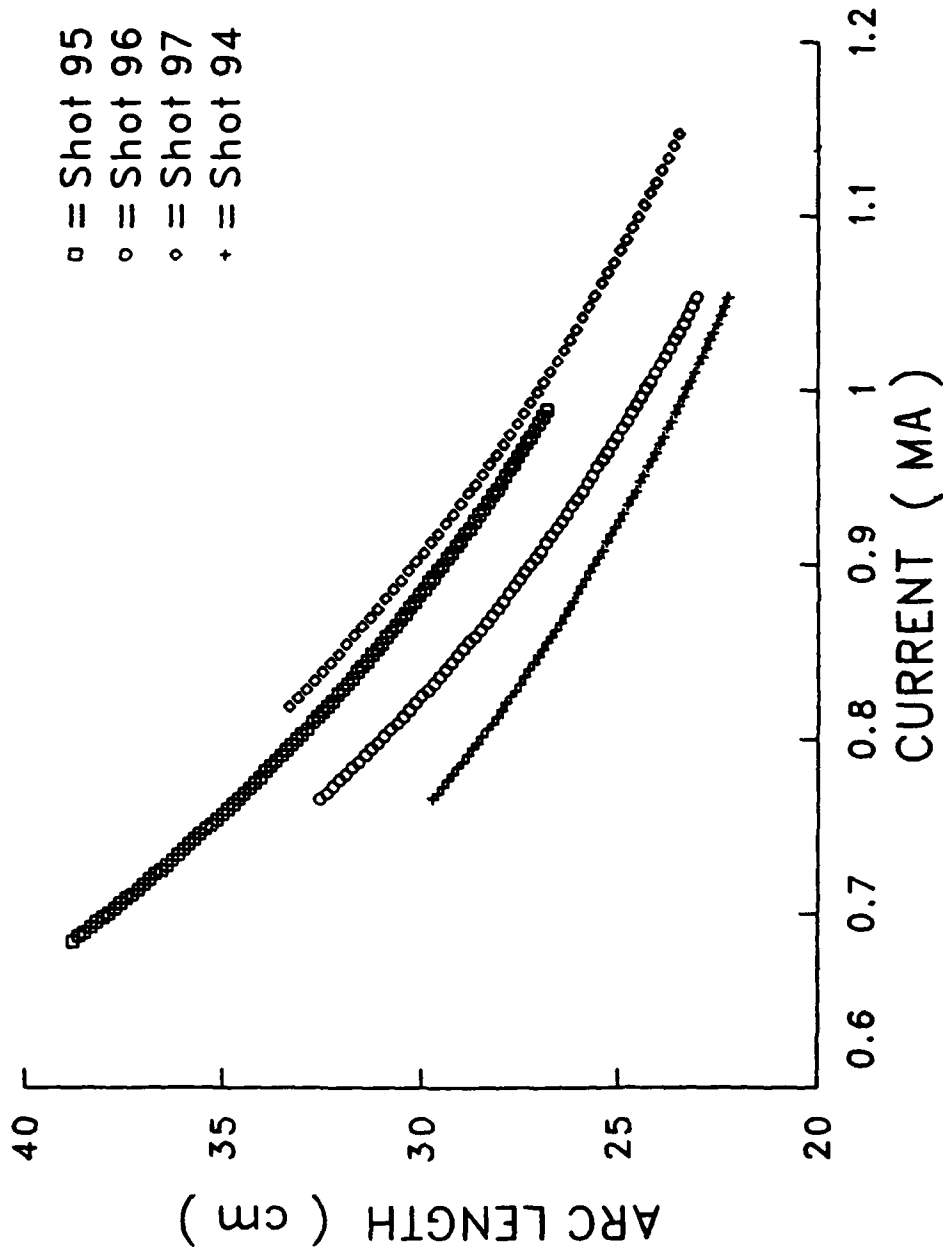


Figure 19. Armature Length Versus Armature Current.
 The length was defined as the distance from the projectile to the point at which J reached one-tenth its maximum value.

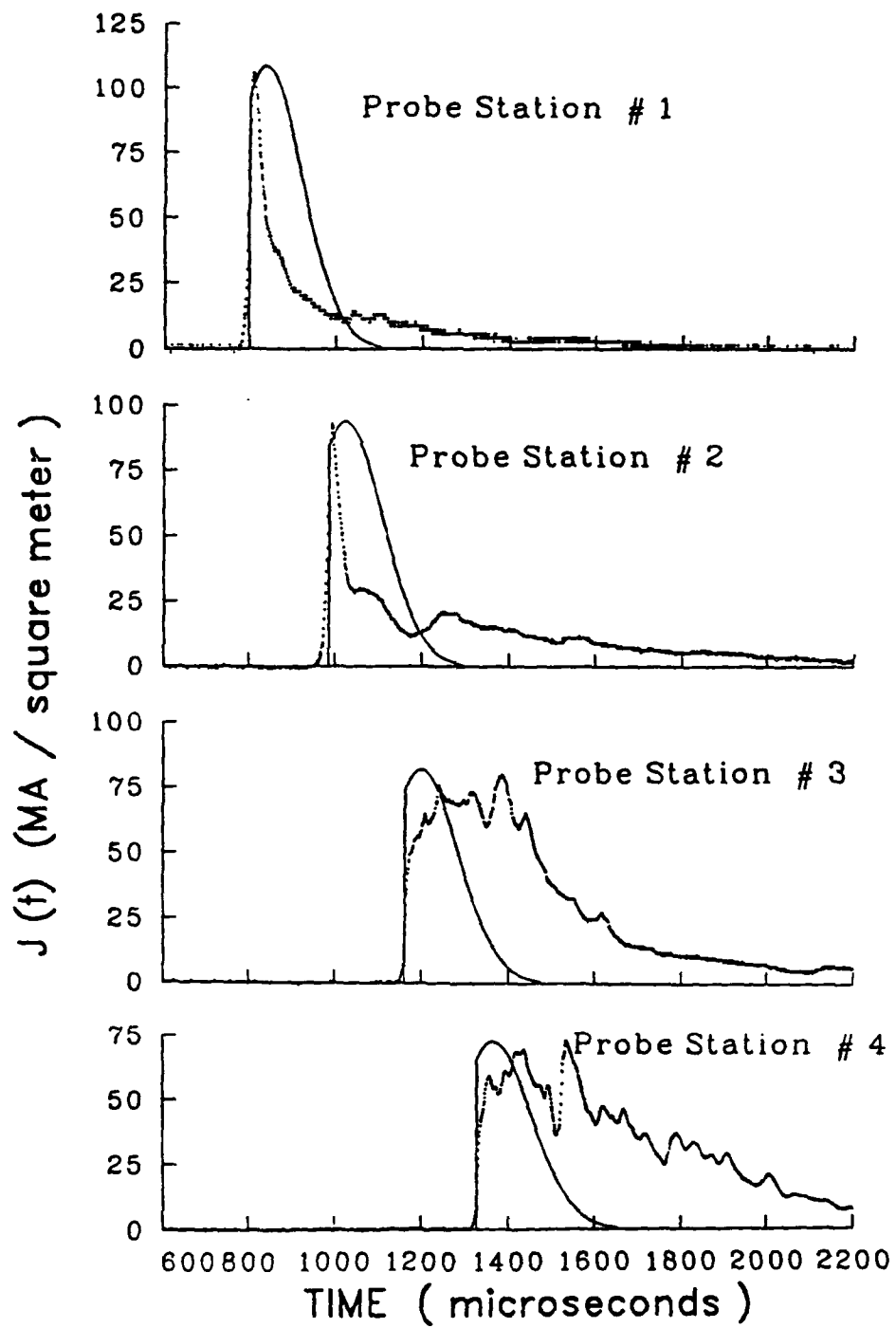


Figure 20. Comparison of Current Density and Light Emission; Shot 95.

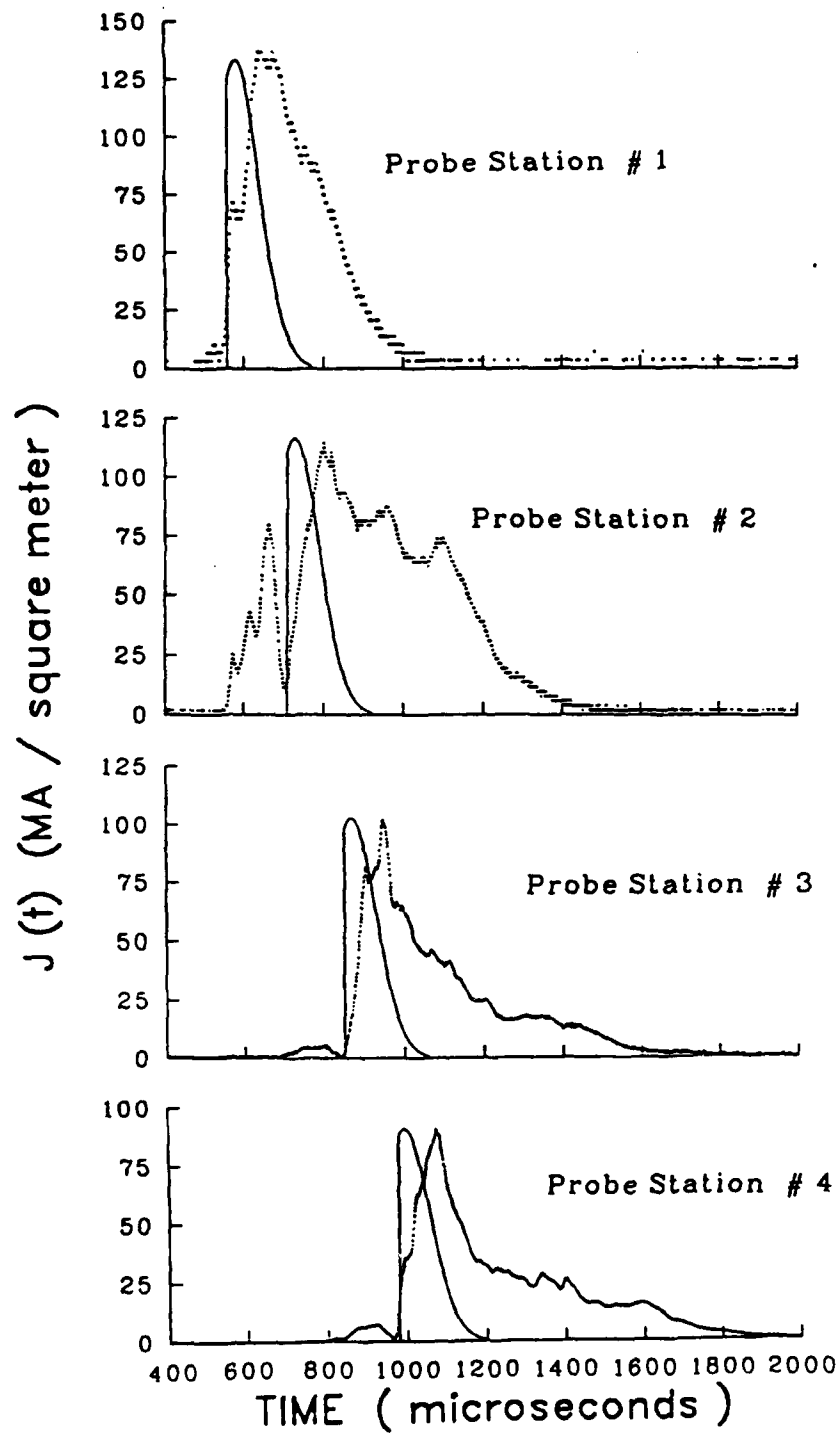


Figure 21. Comparison of Current Density and Light Emission; Shot 96.

III. MODEL CALCULATIONS

In the earlier parts of this report data obtained from several shots on CHECMATE have been discussed in some detail. It is obviously desirable to obtain in addition some estimate of properties of the arc which cannot be measured directly. Such properties include, for example, the arc mass, the temperature as a function of position and time, and the extent of ionization in the arc. In this section of the report we discuss some calculations that we have undertaken to determine these properties.

The model used for the calculations is basically the one-dimensional, steady-state model previously developed by Powell and Batteh.² The model will be applied at each instant of time under the assumption that time-dependent changes in the arc properties occur in a quasi-static manner. This assumption is felt to be reasonable for purposes of analyzing the data discussed here since the arc is rapidly formed and experimental measurements are made well after the acceleration process is underway. If, instead, one wished to study arc formation or, say, the collision of the arc with a projectile, then highly time-dependent effects are important and must be accounted for. These effects have been studied by us¹⁰ and others¹¹ in previous work. There are, of course, additional effects such as instabilities and turbulence, not yet investigated in great detail, and these effects are not included in the model or calculations.

A number of modifications have been made to the steady-state model both to improve the calculations and to make best use of the experimental results. The most significant change is that we have omitted entirely the theoretical calculation of temperature, a calculation previously based on the assumption that ohmic heating in the arc is balanced at any time by radiative cooling. Instead, the temperature within the arc is inferred from the measured (fitted) current density as a function of position and the measured muzzle voltage. This modification has been introduced because theoretical temperature calculations, particularly in one dimension, are not felt to be reliable. Not only are there numerical difficulties, but there may also be additional energy loss/gain mechanisms not accounted for and difficult to quantify. These difficulties are avoided by simply using the experimental data directly. For purposes of comparison, however, we have undertaken some purely theoretical calculations in which temperature is calculated via energy-conservation considerations, and these results will also be discussed in the ensuing pages.

Two other minor modifications have also been introduced. First, the electrical conductivity in the model has been extended to include not only electron-ion scattering (Spitzer), but electron-neutral scattering as well. The latter contribution was included when arc temperatures were found to be

¹⁰Powell, John D. and Jamison, Keith A., "One-Dimensional, Time-Dependent Model for Railgun Arcs," Ballistic Research Laboratory Report No. BRL-TR-2779, Feb 87. See also Jamison, K.A., Burden, H.S., Powell, J.D., and Marquez-Reines, M., "Non-Steady Phenomena in Railgun Plasma Armatures," IEEE Trans. Magn. MAG-22, 1546 (1986).

¹¹Batteh, Jad H. and Rolader, Glenn E., "Modeling of Transient Effects in Railgun Plasma Armatures," Ballistic Research Laboratory Contract Report No. BRL-CR-567, March 1987.

sufficiently low that this scattering mechanism might in some cases be important. The second change in the previously used model is that we have attempted to account very approximately for the finite rail height, h (see Fig. 3). In previous work the rails were assumed to be infinitely high, but this assumption is known to overestimate substantially the acceleration and pressure of the arc. To account for the finite rail height we have used Batteh's approximation¹² in which the magnetic permeability is simply replaced by an effective value.

In Sec. III.1 we outline the governing equations for the model, discussing in particular the changes noted above. In Sec. III.2 we present results of the data analysis, indicating properties of the arc not directly measured, and compare the results with those obtained from some purely theoretical work. We also indicate reasons for the lack of agreement and suggest ways in which future models can be improved.

1. Governing Equations

We take directly from the experimental data at each instant of time values of the muzzle voltage V_m , the arc length l_a , the current i , the projectile location down the bore X_p , and the projectile mass m_p . We also essentially take as given the experimentally determined current-density profile,

$$J = \frac{1}{C} e^{-\frac{(x-x_0)^2}{2W^2}} \quad (6)$$

where values of W and x_0 are also provided by the experiment (see Fig 17). In general, however, theoretical expressions for the arc conductivity vanish at the back of the arc where the density vanishes so that it is convenient to replace Eq. (6) near the back of the arc with a function which vanishes at $x = X_p - l_a$. For simplicity we choose a quadratic function to represent J in this region. In the notation of previous model calculations³ where ξ is a dimensionless distance defined by

$$\xi = \frac{x - X_p + l_a}{l_a} \quad , \quad (7)$$

we therefore have

$$J(\xi) = \frac{1}{C} e^{-\frac{(\xi-\xi_0)^2}{2W_0^2}} \quad , \quad \text{for } \xi > \xi^* \quad (8)$$

$$J(\xi) = C_1 \xi + C_2 \xi^2 \quad , \quad \text{for } \xi < \xi^* \quad .$$

Note that in this notation $\xi = 0$ ($x = X_p - l_a$) corresponds to the trailing edge of the arc and $\xi = 1$ ($x = X_p$) corresponds to the projectile surface. The value of ξ^* is arbitrary, but should be fairly small, and we have consistently chosen $\xi^* = 0.1$. The constants W_0 and ξ_0 in Eq. (8) are given by

¹²Batteh, Jad H., "Momentum Equation for Arc-Driven Rail Guns," J. Appl. Phys. 56, 3182 (1984). See also, "Arc-Dynamic Calculations in the Rail Gun," Ballistic Research Laboratory Contract Report No. ARBRL-CR-00521, Nov 83.

$$W_0 = W/\ell_a$$

and

$$\xi_0 = \frac{x_0 - X_p + \ell_a}{\ell_a} ; \quad (9)$$

the constants C_1 , C_2 and C'_N follow from the requirement that J and $\frac{dJ}{d\xi}$ be continuous at ξ^* and from the current-conservation relation

$$\int_0^1 J d\xi = j/\ell_a . \quad (10)$$

Here j is the rail current per unit height. We easily determine from these conditions that

$$C'_N = \frac{2\ell_a \xi^* R_1}{3j} - \frac{\ell_a \xi^* R_2}{6j} + \frac{W_0 \ell_a}{j} \left(\frac{\pi}{2}\right)^{1/2} \left[\operatorname{erf} \left(\frac{1-\xi_0}{\sqrt{2} W_0}\right) - \operatorname{erf} \left(\frac{\xi^*-\xi_0}{\sqrt{2} W_0}\right) \right] \quad (11)$$

$$C_1 = \frac{2R_1}{C'_N \xi^*} - \frac{R_2}{C'_N} , \quad (12)$$

and

$$C_2 = \frac{R_2}{C'_N \xi^*} - \frac{R_1}{C'_N \xi^{*2}} . \quad (13)$$

In these expressions

$$R_1 = e^{-(\xi^* - \xi_0)^2 / 2W_0^2} ,$$

$$R_2 = -\frac{(\xi^* - \xi_0)}{W_0^2} e^{-(\xi^* - \xi_0)^2 / 2W_0^2} \quad (14)$$

and $\operatorname{erf}(x)$ is the error function

$$\operatorname{erf}(x) = \frac{2}{\sqrt{\pi}} \int_0^x e^{-u^2} du . \quad (15)$$

Once the current density has been obtained, expressions for the magnetic-induction field B and pressure P follow immediately from results derived in Ref. 2. In particular, we have

$$B(\xi) = \mu j - \mu \ell_a \int_0^\xi J(\xi) d\xi , \quad (16)$$

which yields after employing (8) and integrating

$$B(\xi) = \mu j - \mu l_a (C_1 \xi^2/2 + C_2 \xi^3/3) , \text{ for } \xi < \xi^*$$

and

(17)

$$B(\xi) = \mu j - \mu l_a (C_1 \xi^{*2}/2 + C_2 \xi^{*3}/3) - \frac{\mu l_a W_0}{C_N} \left(\frac{\pi}{2}\right)^{1/2} \left[\operatorname{erf} \left(\frac{\xi - \xi_0}{\sqrt{2} W_0} \right) - \operatorname{erf} \left(\frac{\xi^* - \xi_0}{\sqrt{2} W_0} \right) \right], \text{ for } \xi > \xi^* .$$

If we further assume that the projectile mass is large compared to the arc mass, as we will find to be the case in all our analysis, then the hydrostatic pressure P is given in terms of the B field by

$$P = \frac{\mu j^2}{2} - \frac{B^2}{2\mu} . \quad (18)$$

In Eqs. (16)-(18), μ is the standard, free-space, magnetic permeability. These equations, however, have been derived under the assumption that the rails are infinitely high, an approximation that is known to overestimate the pressure and accelerating force of the arc.² Batteh¹² has argued that approximate account can be taken of finite rail height provided μ in these equations is replaced by an effective value μ^* . In a tedious calculation he has worked out the appropriate value and finds

$$\mu^* = \frac{2\mu}{\pi S} [S \tan^{-1}(S) + S^2/4 \log(1 + 1/S^2) - \frac{1}{4} \log(1 + S^2)] \quad (19)$$

where $S = h/w$, i.e., the ratio of the rail height to rail separation. We will employ this approximation in the remainder of our analysis.

The position-dependent conductivity within the arc can also be inferred from the experimental data, namely, the current density in (6) and the measured muzzle voltage. It has been noted¹⁰ that in the steady state J/σ is independent of position in the arc and is given by

$$J/\sigma = V_p/w . \quad (20)$$

Here σ is the arc conductivity and V_p is the potential drop across the plasma. Consequently, we have

$$\sigma = wJ/V_p . \quad (21)$$

In terms of the measured voltage V_m , V_p is given by

$$V_p = V_m - V_c \quad (22)$$

where V_c is the total contact potential at the two rail-arc interfaces. Unfortunately, values of V_c are not known, so we have analyzed the data for various reasonable estimates.

The remaining properties of the arc that must be determined are the temperature T , the concentration of singly and doubly charged ions x_1 and x_2 , the density ρ , and finally the arc mass m_a . To determine the first three of these quantities we invoke the theoretical expression for the arc conductivity along with the Saha equations which predict the ionization state as a function of temperature and pressure. For the conductivity we assume¹³

$$\frac{1}{\sigma} = \frac{1}{\sigma_L} + \frac{1}{\sigma_H} \quad (23)$$

where σ_H is the conductivity of a completely ionized gas and σ_L that for a slightly ionized gas. For σ_H the standard Spitzer expression is used

$$\sigma_H = \frac{2.3 \times 10^{-2} \gamma_E}{Z \log \Lambda} T^{3/2} \quad (24)$$

where Z is

$$Z = \frac{x_1 + 4x_2}{x_1 + 2x_2} \quad (25)$$

and γ_E is a constant given by 0.587 for a singly ionized gas and by 0.683 for a doubly ionized gas. For arbitrary ionization we have assumed for simplicity a linear relation

$$\gamma_E = 0.096 Z + 0.491 \quad (26)$$

The shielding parameter Λ in Eq. (24) can be written in terms of T , P , x_1 and x_2 as

$$\Lambda = \frac{1.23 \times 10^7 T^{3/2}}{Z} \frac{(1 + x_1 + 2x_2) k_B T^{1/2}}{P(x_1 + 2x_2)} \quad (27)$$

where k_B is Boltzmann's constant.

For the case of slight ionization we use the relation

¹³Cambel, A.B., Plasma Physics and Magnetofluidmechanics (Mc-Graw-Hill, New York, 1963), Chap. 7.

$$\sigma_L = \frac{4.5 \times 10^{-12} (x_1 + 2x_2)}{(1 - x_1 - x_2) Q T^{1/2}} \quad (28)$$

where Q is the electron-neutral scattering cross section. Values of Q are generally not known in all temperature ranges for materials of interest so we have assumed a constant value of 10^{-18} m^2 . At most temperatures σ is not a particularly sensitive function of Q .

The ion concentrations x_1 and x_2 follow from solutions to the Saha equations as discussed in Ref. 2. Thus, we have the relations

$$\frac{x_1 (x_1 + 2x_2)}{(1 - x_1 - x_2)(1 + x_1 + 2x_2)} = K_1 (T, P)$$

and (29)

$$\frac{x_2 (x_1 + 2x_2)}{x_1 (1 + x_1 + 2x_2)} = K_2 (T, P) .$$

Calculation of the functions K_1 and K_2 has been discussed elsewhere² and will not be discussed here. We should point out, however, that these functions depend only on the temperature and pressure and on the the properties of the material which constitutes the arc, i.e., the ionization potentials and electronic partition functions.

It is now apparent that Eqs. (23) and (29) along with the supplementary relations discussed and the experimentally inferred conductivity can be solved simultaneously to yield values of T , x_1 , and x_2 at all points of the arc. This solution must be carried out numerically. Once the values are known, however, the density follows from the ideal-gas equation of state assumed in all our previous work, namely,

$$\rho = \frac{m_0 P}{(1 + x_1 + 2x_2) k_B T} \quad (30)$$

where m_0 is the atomic mass of the ions or neutrals making up the arc. Finally, the arc mass follows directly from the calculated density and measured arc length via the relation

$$m_a = h w \ell_a \int_0^1 \rho(\xi) d\xi \quad (31)$$

where h is the rail height.

The foregoing analysis is sufficient to determine all the arc properties without our having to employ any relationship relating to energy conservation. We now turn to a discussion of some of the calculations.

2. Results of Calculations

We have undertaken numerous calculations using the formalism of the preceding section and discuss here only some of the more typical results. The calculations fall basically into two groups. In the first, certain average or position-independent properties of the arc were computed; in the second, spatially dependent quantities were calculated at a given point in time. All data were taken from three of the shots on CHECMATE discussed previously, those numbered 95, 96 and 97. The projectile mass for Shots 95 and 97 was 233g, while that for Shot 96 was 120g.

The material which constitutes the arc was not, of course, known in any detail and most of our results are based on the assumption that it consists of carbon vapor. Carbon was chosen for most of the calculations for reasons which will be explained when the analysis is presented. We have, however, undertaken some computations for copper and aluminum-vapor arcs and these results are briefly discussed primarily to indicate some of the more salient differences. We have also assumed in most calculations that no contact potential existed at the rail-arc interfaces. Thus, the total measured muzzle voltage in Eq. (22) is assumed to be a bulk voltage drop across the plasma. We do, however, indicate in some of the later discussion what effect a nonzero contact potential should have and how it can bring experimental and theoretical results into better agreement.

Shown in Fig. 22 is the calculated armature mass for the carbon arc as a function of time for each of the three shots. For Shots 95 and 97 the mass appears to remain nearly constant at about 1.5g for the entire acceleration time. Thus, if a significant amount of ablation is occurring during the shot, the resulting mass does not appear to be entrained in the arc. This point will be discussed further when a comparison with some purely theoretical results is made. For Shot 96 the arc mass is slightly smaller than for the other two cases. One possible explanation for the slightly smaller mass in Shot 96 is that the injection velocity for this case (smaller projectile mass) is higher than that for Shots 95 and 97 and the dwell time at any given point on the rails is also smaller. Consequently, less time is available for rail and insulator material to become vaporized and entrained in the arc if in fact such an effect occurs at very early times before the nearly steady values, seen in Fig. 22, are achieved. It should also be noted that there are fairly significant drops in the armature mass at about 0.7 and 0.9 milliseconds. These times are just subsequent to the times at which light-output data from Shot 96 indicated luminous material being blown past the projectile (see Sec. II.2.d). At each time, however, the equilibrium value of the mass appears to be quickly restored.

We have also computed as a function of the pulsed current i both mean and peak temperatures within the arc as well as the mean concentration of single ions $\langle x_1 \rangle$. The peak temperature occurs just to the left of the projectile surface as will be seen when some spatially dependent results are presented. These results are shown in Figs. 23-25 and exhibit largely self-explanatory behavior. Both temperature profiles increase with increasing

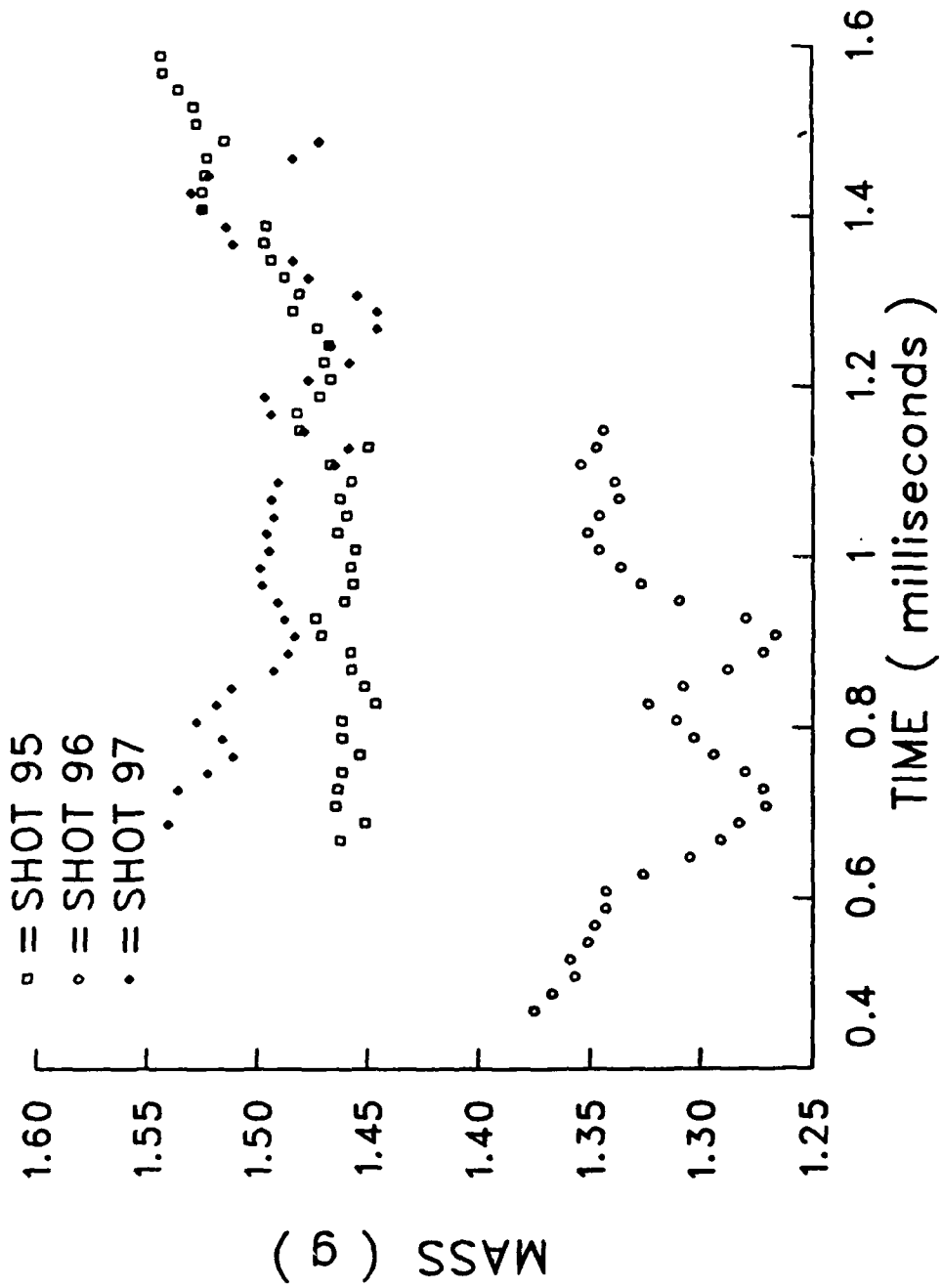


Figure 22. Calculated Armature Mass Versus Time of the Carbon Arc.

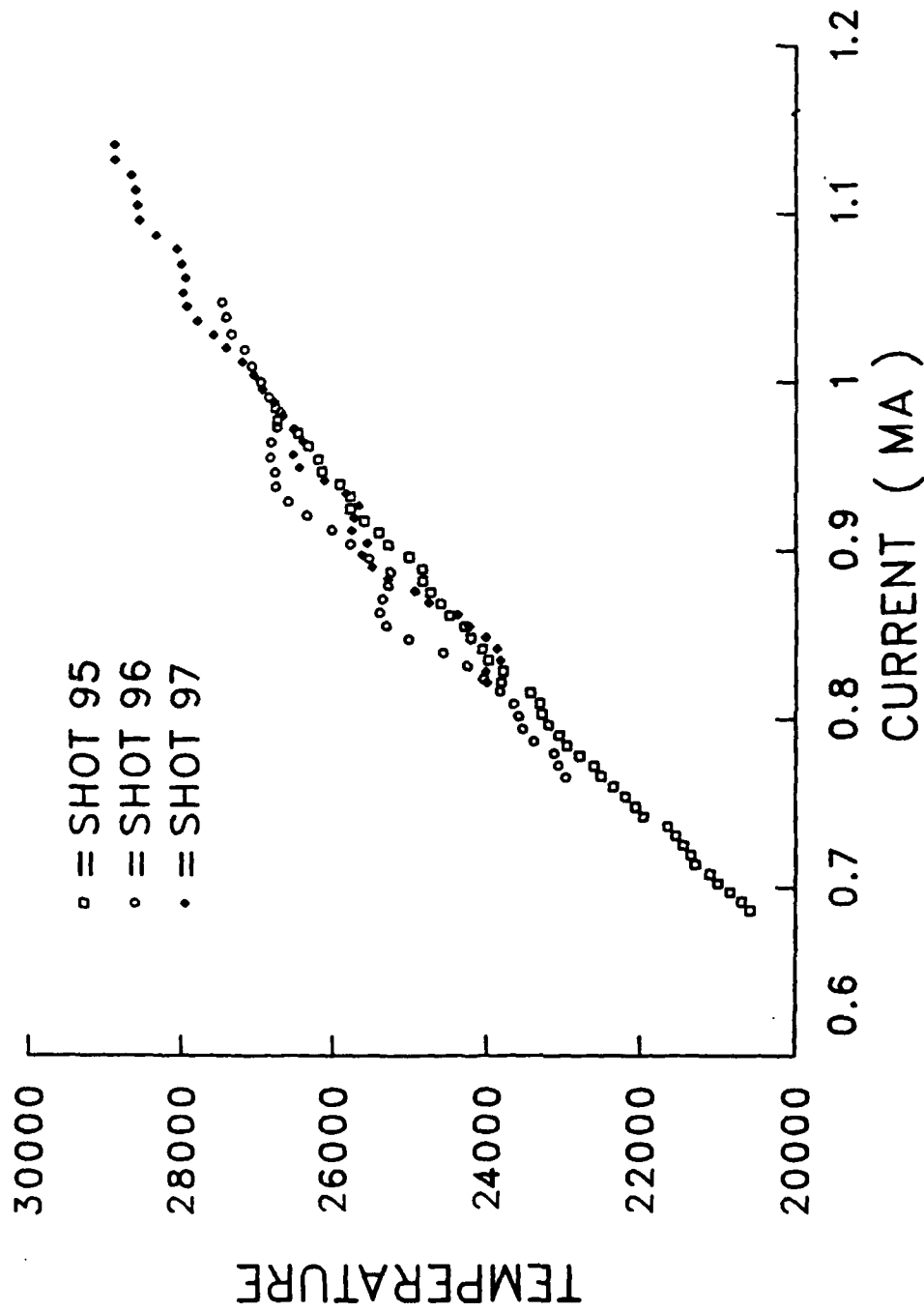


Figure 23. Peak Temperature Versus Current for Carbon Arc.

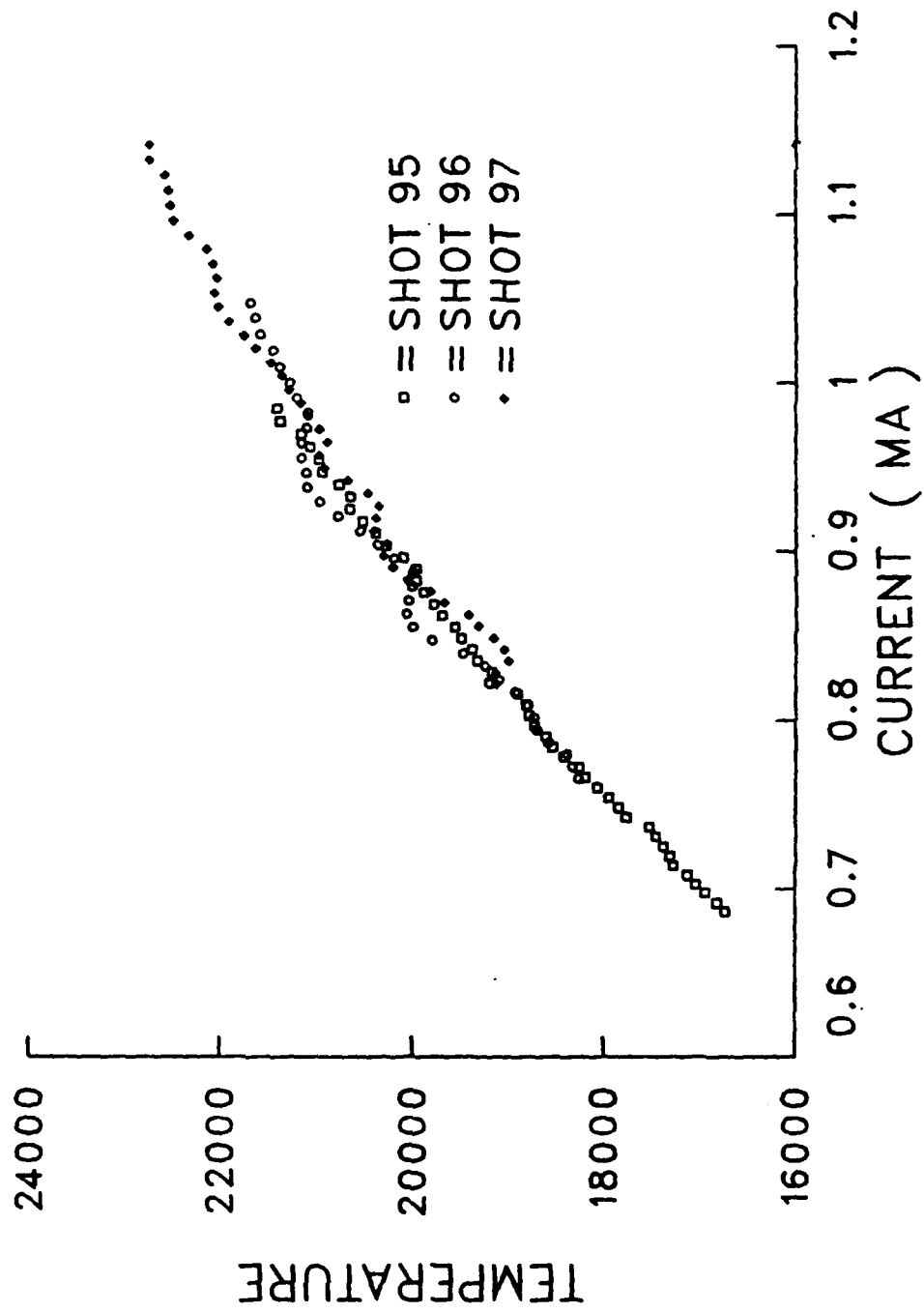


Figure 24. Average Temperature Versus Current for Cabron Arc.

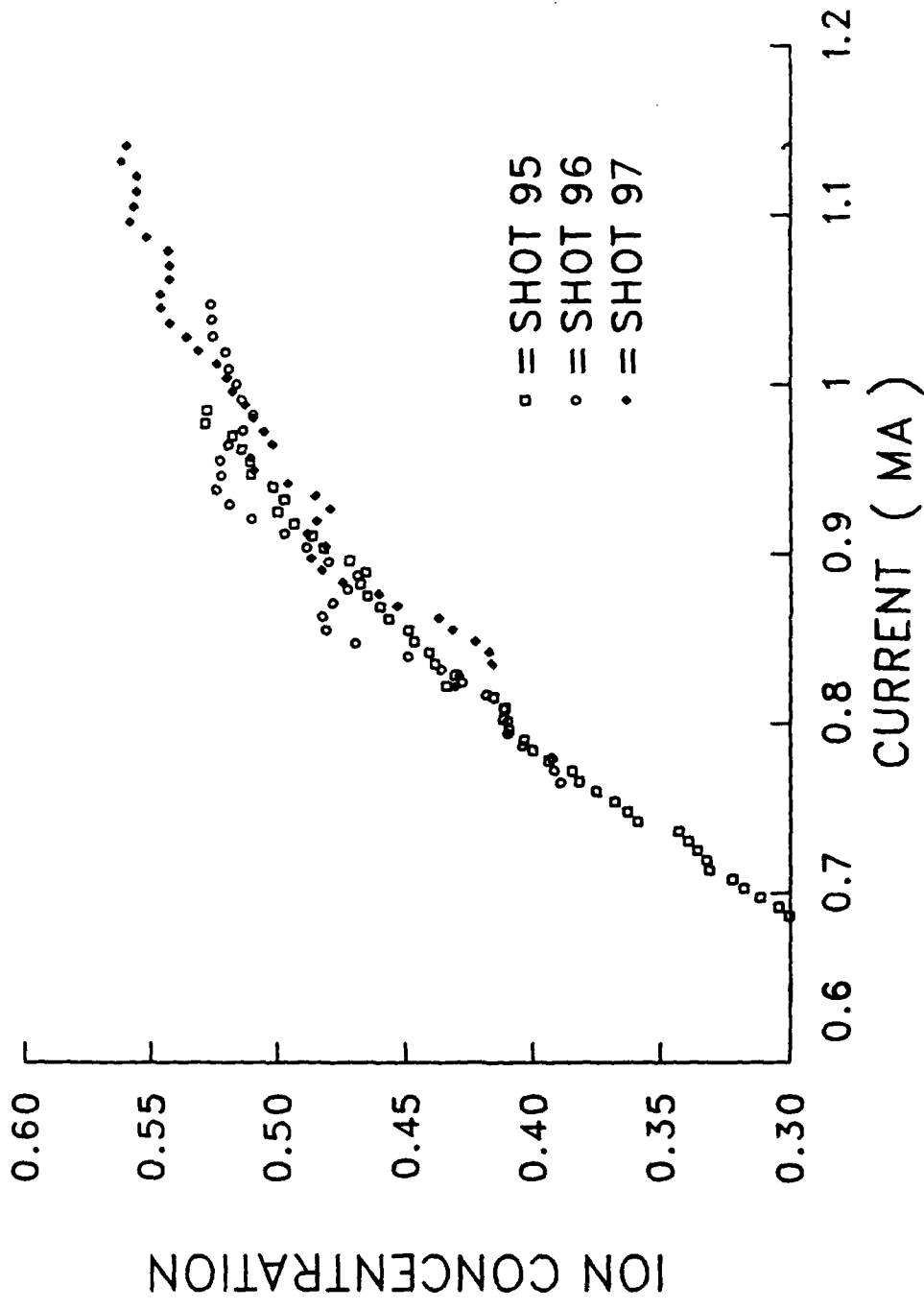


Figure 25. Average Ion Concentration Versus Current for Carbon Arc.

current, the increase resulting primarily from enhanced ohmic heating at higher currents. It is of interest to note that very approximate scaling relations,³ derived under the assumption that $w \ll \lambda_a$, indicate that temperature should increase as $I^{6/11}$. The graphs in Figs. 23 and 24 can be seen to obey roughly such a relation.

The mean concentration of single ions can also be seen to increase with increasing current. Basically, this behavior results from competition between the increasing temperature, which enhances ionization, and the increasing pressure, which reduces it. The ionization degree, however, is a very sensitive function of temperature, and a much less sensitive function of pressure. The concentration of doubly charged ions was also computed but, at these relatively low temperatures, their values were too small to be evident on the graph.

It is also of interest to ask to what extent the results of the data analysis are in agreement with results from purely theoretical calculations. We have therefore exercised our one-dimensional model to undertake a number of calculations pertinent to the experimental results. For these model calculations it is necessary to specify only the arc length λ_a , the projectile mass m_p , and the current I . All remaining quantities are then calculated as a function of position within the arc. In particular, temperature is calculated by the energy-conservation assumption that ohmic heating is balanced at any time by radiation. Radiation losses are represented in the manner discussed in Ref. 2 except that here we have scaled the resulting temperatures down by the factor $(A_E/A_A)^{3/4}$ where A_E is the surface area of the ends of the arc and A_A is the surface area of the total arc. This scaling was performed because a truly one-dimensional model, which accounts for only losses at the ends, is known to overestimate substantially the arc temperature. More sophisticated approximations, accounting for losses from the sides, have also been undertaken but this simple scaling procedure appears to be nearly as accurate as any of them and is very simple to employ.

Shown in Fig. 26, Curve A, and in Table V are the theoretical results² for the temperature as a function of position within the arc using as input the parameters: $I = 903$ kA, $\lambda_a = 29$ cm, and $m_p = 0.233$ kg. These parameters were taken directly from the experimental data^p for Shot 95 at the time $t = 0.89$ ms. The theoretical temperature profile is similar to that we have observed in previous model calculations. The temperature peak occurs just to the left of the projectile and steep gradients exist near the projectile surface. The steep gradients result from the high density and consequent small radiation mean free path in this region. In essence, photons are "trapped" behind the projectile and can radiate outward only when they are within a mean free path or so of the boundary.

In the theoretical models no account is taken of any contact potential at the rail-arc interfaces so that only the potential drop across the plasma, V_p , is calculated. This potential is equivalent to the experimentally measured muzzle voltage V_m only if negligible contact potential really exists. Otherwise, the contact potential V_c should be subtracted from the muzzle voltage V_m before a comparison with the theoretical results is undertaken. Since numerical values of the contact potential are not known, we have carried out the data analysis in Fig. 26 for three different values of V_c , namely, 0, 75 volts and 167 volts, shown in curves B, C and D, respectively. The last value

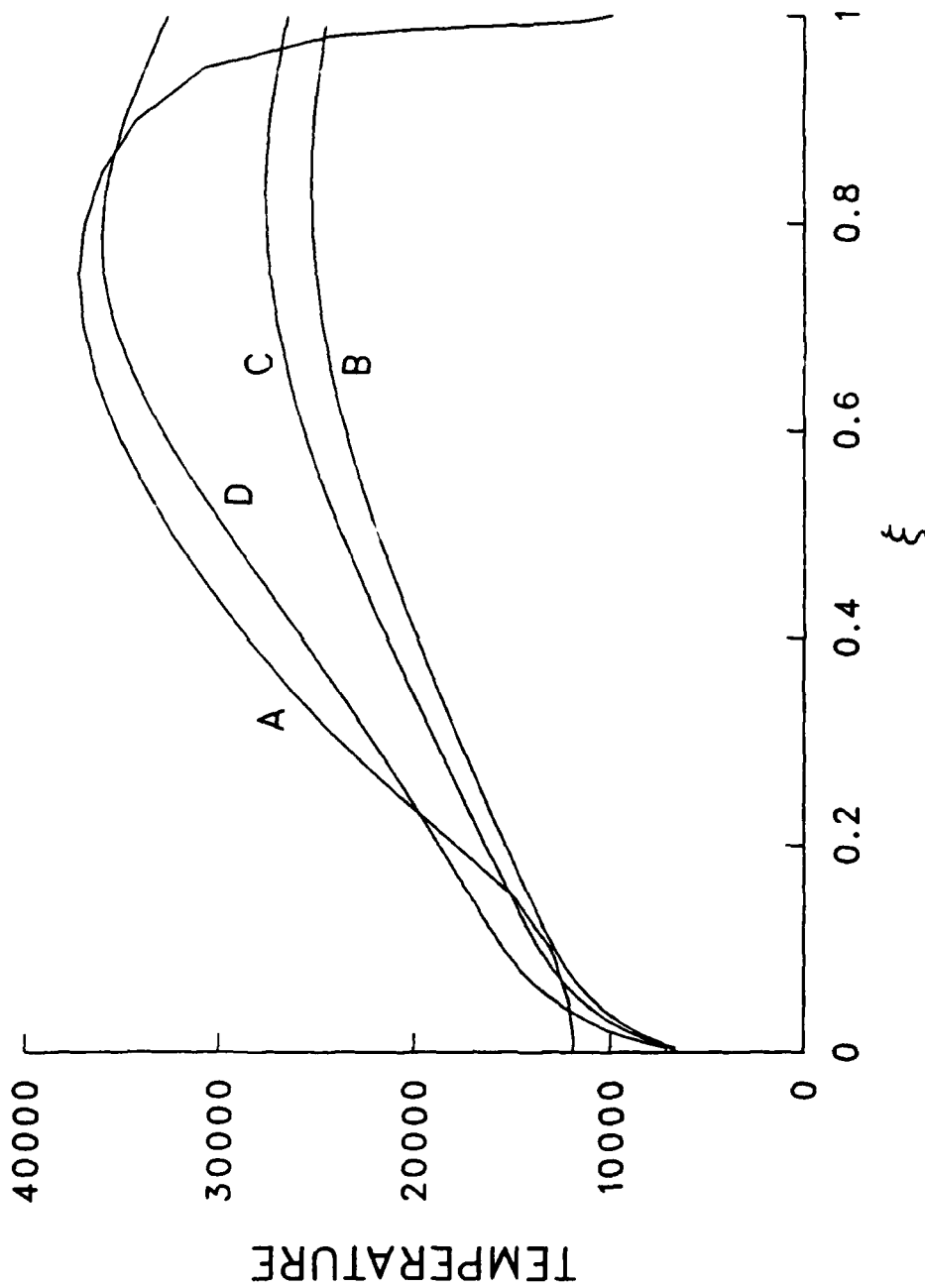


Figure 26. Comparison of Temperatures for Carbon Arc from Data Analysis and Theory. A, theoretical; B, data analysis for $V_c = 0$; C, data analysis for $V_c = 75$ V; D, data analysis for $V_c = 167$ V.

was chosen so that the potential drop across the plasma V_p was the same as the value predicted from the theory.

TABLE V. Comparison of Theoretical and Data Analysis Results

	A	B	C	D
m_a	0.95 g	1.46 g	1.25 g	0.87 g
V_m	-	287V	287V	287V
V_c	-	0	75V	167V
V_p	120V	287V	212V	120V
$\langle T \rangle$	2.77×10^4	2.03×10^4	2.19×10^4	2.72×10^4
T_{MAX}	3.74×10^4	2.52×10^4	2.76×10^4	3.62×10^4
$\langle X_1 \rangle$	0.74	0.48	0.59	0.77
$\langle X_2 \rangle$	0.034	0.003	0.004	0.025

It is evident from Fig. 26, curves A and B, that there is substantial disparity between theory and experiment if one assumes that no contact potential exists at the rail-arc interfaces; at some points the two temperatures differ by as much as 50%. As V_c increases, however, as shown in curves C and D, the experimental temperatures also increase and approach the theoretical profile. The increase in T with increasing V_c results from the consequent smaller values of V_p . These smaller values can result only if the conductivity, and thus the temperature, also increases. It seems probable that the contact potential lies somewhere between the extreme values of 0 and 167 volts so that a realistic curve from the data analysis, accounting accurately for the contact potential, would still lie somewhat below the theoretical profile. If so, it appears that the theory probably overestimates the temperature of the arc by a few percent. One likely source of error in the model is the neglect of some energy-loss mechanism. Recently, it has been proposed that neutral atoms may diffuse out the back of the arc, while mass is added via ablation in such a way that the total arc mass remains nearly constant. If so, the neutrals will carry energy with them and this loss mechanism is not presently accounted for in the theory. That there is high concentration of neutrals near the back of the arc can be seen in Fig. 27 in which the neutral concentration, averaged over the back 25% of the arc, is plotted as a function of current. The data used to compute this curve are identical to those used in the computation of results in Figs. 22-24. It seems unlikely that such large numbers of neutrals, particularly at low currents, could be carried along with the arc without some significant loss out the back.

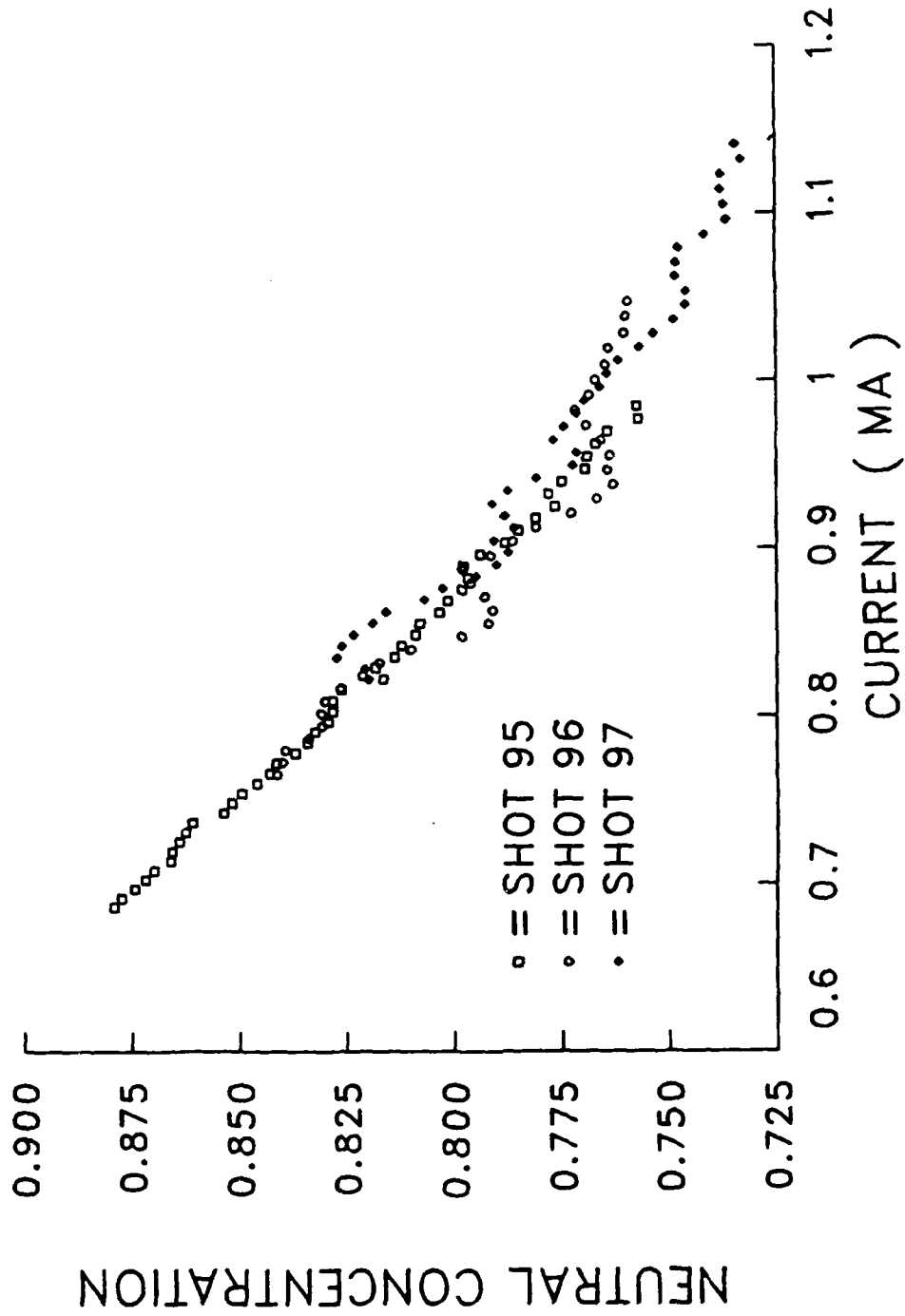


Figure 27. Neutral Concentration Averaged over Trailing Edge of Carbon Arc.

Unfortunately, we cannot determine unequivocally the cause for the discrepancy between the theoretical and experimental temperature profiles. No doubt both effects discussed in the preceding paragraph contribute to some extent to the lack of agreement. Crude estimates which we have made suggest that the energy lost via neutral diffusion is probably fairly small (at most of the order of 10% of the arc's internal energy) but these studies require more analysis. We are not aware of any reliable estimates, theoretical or experimental, of the contact potential.

We should also point out that it would obviously be more desirable to compare results of the data analysis with theoretical calculations obtained from a model in which the contact potential was specifically included. One could then determine to what extent the existence of such a potential affected the internal properties of the plasma. Unfortunately, no such model exists. It does seem reasonable, however, to expect that such effects would not be too significant since the potential is localized near the rail surfaces. Further, studies are nonetheless appropriate when the nature and magnitude of the contact potential are better understood.

We have also carried out some calculations under the assumption that the arc was composed of aluminum and copper ions. A summary of the results of these calculations is indicated in Figs. 28 and 29 in which we have plotted as a function of current the arc mass m_a and the mean temperature T for the three different types of arc materials. All data were taken from Shot 95 so that the curves for carbon were shown in Figs. 22 and 24. For reference the first and second ionization potentials and atomic masses of the materials involved are shown in Table VI. As can be seen in Fig. 28, the masses of the different arcs are substantially different and scale very roughly with the atomic mass. Furthermore, it is noteworthy that the mass computed for the aluminum arc ($\approx 4g$) is significantly higher than was the mass of the fuse initially blown to create the arc ($\approx 0.3g$). Since no other source of aluminum was present, it then appears that only a very small percentage of the arc actually consists of aluminum vapor. Similar statements cannot be made about the other materials. However, since copper has a thermal conductivity higher than the insulating material, and is therefore harder to vaporize, it appears likely that the arc is composed primarily of elements from the insulators, i.e., carbon, hydrogen and oxygen. The temperatures of the various arcs are not nearly so different as their masses but in general increase with increasing ionization potential. The result can be understood if it is remembered that all three arcs have a common conductivity and pressure and thus higher temperatures are needed to ionize the materials which have higher ionization potentials. However, the extent of ionization is a sensitive function of the temperature so fairly small changes in this parameter mean large changes in ion concentration.

TABLE VI. Ionization Potentials and Atomic Masses of Arc Materials

<u>Material</u>	<u>I_1(ev)</u>	<u>I_2(ev)</u>	<u>m_0(amu)</u>
C	11.26	24.38	12
Al	5.98	18.82	27
Cu	7.72	20.29	64

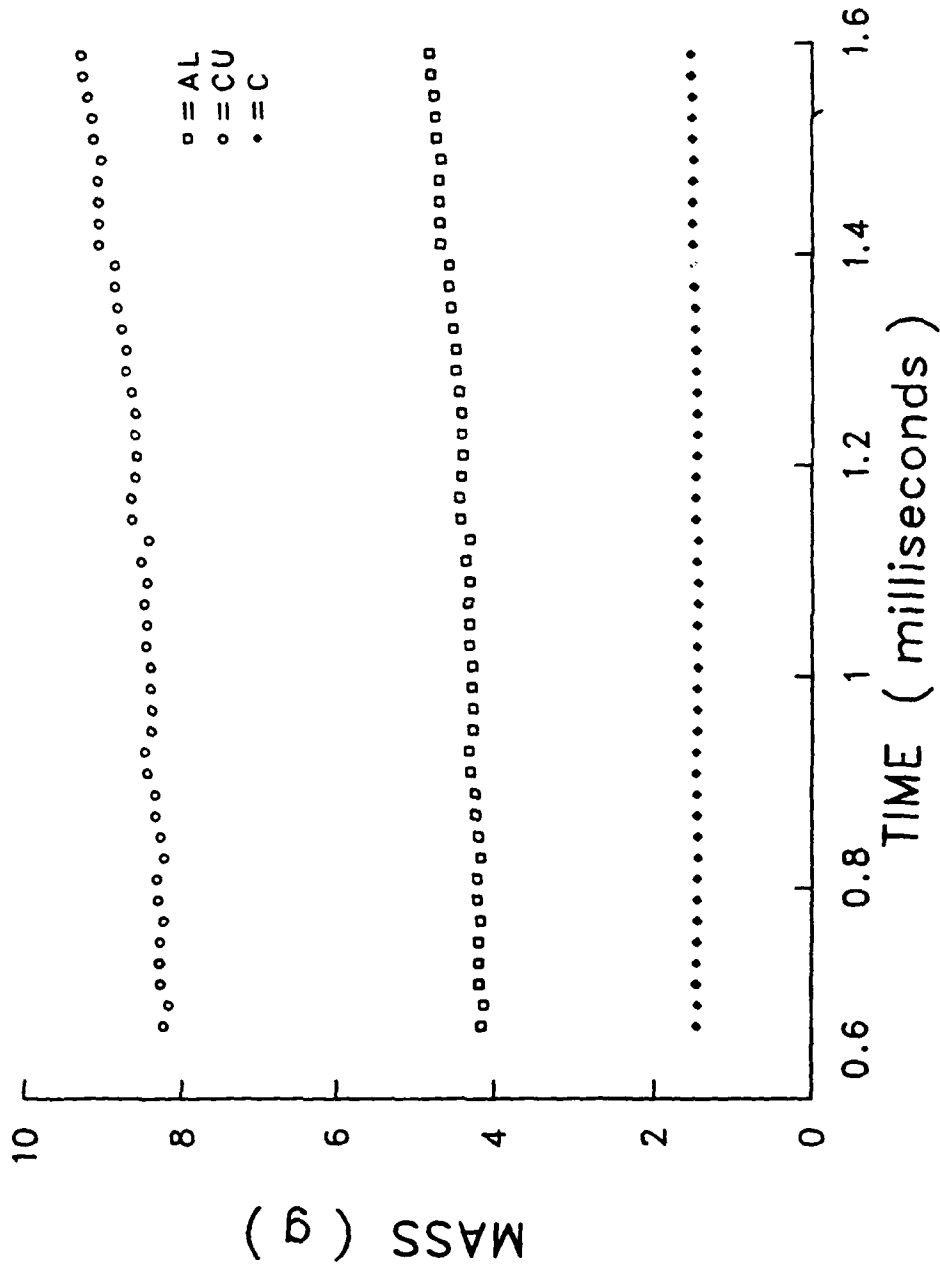


Figure 28. Armature Mass Versus Time for Different Arc Materials.

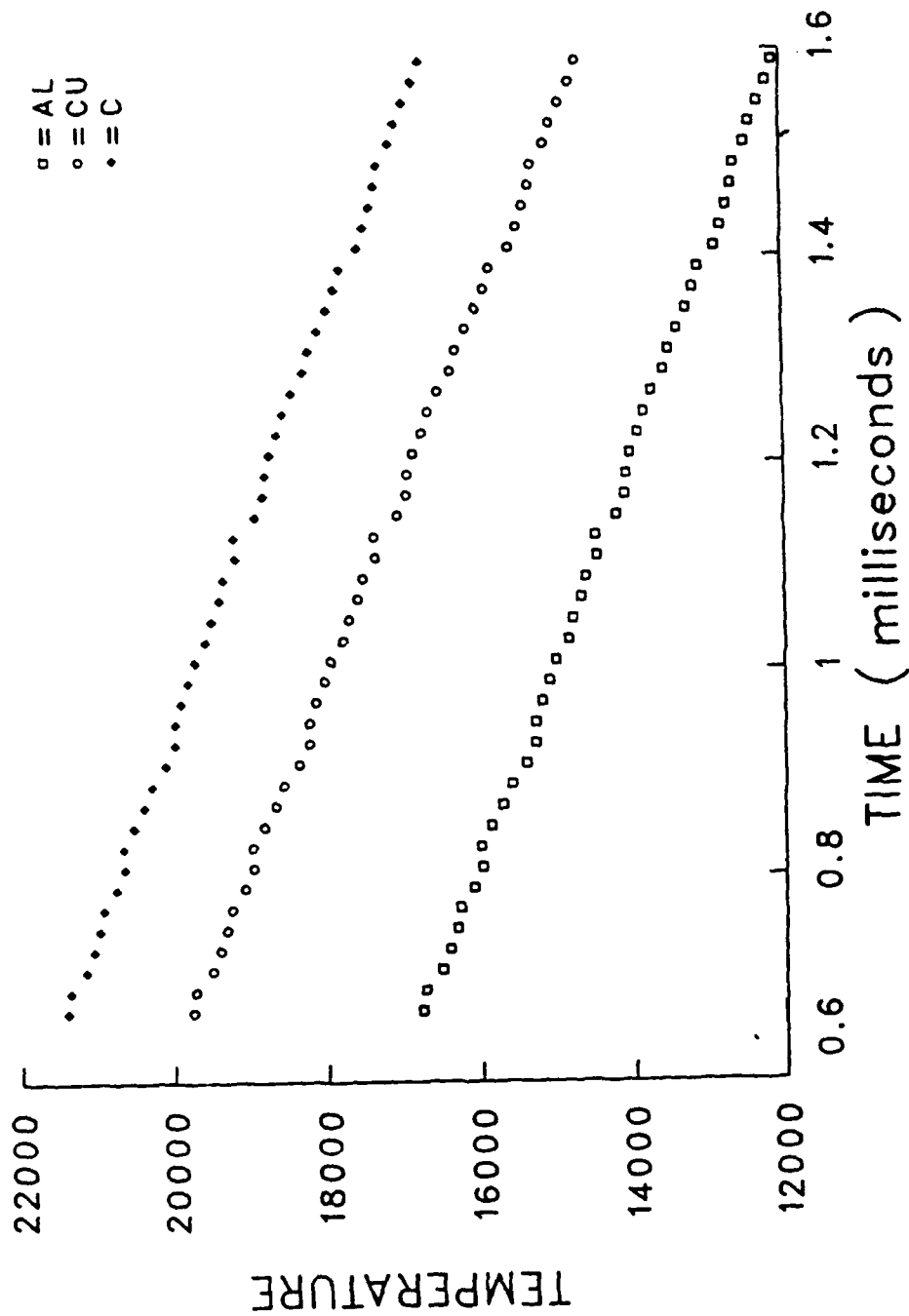


Figure 29. Mean Arc Temperature Versus Time for Different Arc Materials.

IV. CONCLUSIONS AND RECOMMENDATIONS

The diagnostic measurements and analysis undertaken here have led to a number of conclusions concerning plasma arcs in large-bore railguns. These conclusions may be summarized as follows. First, it appears that the total mass of the arc remains nearly constant over the acceleration time. Such an effect could occur if there were no ablation from the rails or insulators and, in addition, no mechanism for losing mass from the arc. It is more likely, however, that some ablation does occur, particularly from the insulating materials, and the resulting increase in mass is compensated for by some loss mechanism. Two possible mechanisms are diffusion of neutrals out the back of the arc and losses at boundary layers whose velocity must vanish at the rail surface.¹⁴ Both these problems merit further study as do efforts to quantify the extent of ablation as a function of the other arc properties.

Second, it appears that theoretically derived temperatures are still significantly higher than those inferred from experiment. This observation persists even though the one-dimensional, theoretical model has been revised to account approximately for radiation losses from the sides of the arc. It is possible that the theoretical results fail to account for some energy-loss mechanism (such as would accompany the mass loss described above) and thus overestimate the temperature. It is also possible, however, that there is a significant contact potential at the rail-arc interfaces so the measured muzzle voltages are much higher than the potential drop across the plasma. As has been seen, postulating a contact potential and subtracting its value from the muzzle voltage before undertaking the data analysis leads to substantially better agreement of theory and experiment. Undoubtedly, both these factors are present and the extent of each can be determined only by further study. Of particular importance are experimental efforts to measure the contact potential and theoretical studies of the mass diffusion postulate.

Finally, it does not appear possible to gain much information concerning the composition of the arc from the work undertaken here. It is fairly evident that there is very little aluminum present but the dominant material cannot be inferred. Presumably, the arc is formed at very early times, before its apparently steady mass is achieved, by material ablated from the projectile, rails, or insulators. Experimental efforts to determine the composition of the arc would obviously be worthwhile and, then, theoretical models could be revised to account for the appropriate mixture. It does appear, however, that many arc properties are not significantly affected as the arc composition is varied among several reasonable alternatives.

¹⁴Barber, John P., private communication.

REFERENCES

1. Holland, M.M., Wilkinson, G.M. Krickhuhn, A.P., and Dethlefsen, R., "Six Megajoule Rail Gun Test Facility," IEEE Trans. Magn. MAG-22, 1521 (1986).
2. Powell, John D. and Batteh, Jad H., "Plasma Dynamics of an Arc-Driven Electromagnetic Projectile Accelerator," J. Appl. Phys. 52, 2717 (1981). See also, "Plasma Dynamics of the Arc-Driven Rail Gun," Ballistic Research Laboratory Report No. ARBRL-TR-00267, September 1980.
3. Powell, John D. and Batteh, Jad H., "Two-Dimensional Plasma Model for the Arc-Driven Railgun," J. Appl. Phys. 54, 2242 (1983). See also, Powell, John D., "Two Dimensional Model for Arc Dynamics in the Railgun," Ballistic Research Laboratory Report No. ARBRL-TR-02423, October 1982.
4. Sloan, M.L., "Physics of Rail Gun Plasma Armatures," IEEE Trans. Magn. MAG-22, 1747 (1986).
5. Thio, Y.C. and Frost, L.S., "Non-Ideal Plasma Behavior of Railgun Arcs," IEEE Trans. Magn. MAG-22, 1757 (1986).
6. Jamison, K.A. and Burden, H.S., "A Laboratory Arc Driven Rail Gun," Ballistic Research Laboratory Report No. ARBRL-TR-02502, June 1983.
7. Wilkinson, G.M. (unpublished data).
8. Jamison, K.A., Marquez-Reines M. and Burden, H.S., "Measurement of the Spatial Distributions of Current in a Rail Gun Arc Armature," IEEE Trans. Magn. MAG-20, 403 (1984).
9. Powell, John D., "Interchange Instability in Railgun Arcs," Phys. Rev. A, 34, 3262 (1986). See also, Ballistic Research Laboratory Report No. BRL-TR-2776, January 1987.
10. Powell, John D. and Jamison, Keith A., "One-Dimensional, Time-Dependent Model for Railgun Arcs," Ballistic Research Laboratory Report No. BRL-TR-2779, Feb 87. See also Jamison, K.A., Burden, H.S., Powell, J.D., and Marquez-Reines, M., "Non-Steady Phenomena in Railgun Plasma Armatures," IEEE Trans. Magn. MAG-22, 1546 (1986).
11. Batteh, Jad H. and Rolader, Glenn E., "Modeling of Transient Effects in Railgun Plasma Armatures," Ballistic Research Laboratory Contract Report No. BRL-CR-567, March 1987.
12. Batteh, Jad H., "Momentum Equation for Arc-Driven Rail Guns," J. Appl. Phys. 56, 3182 (1984). See also, "Arc-Dynamic Calculations in the Rail Gun," Ballistic Research Laboratory Contract Report No. ARBRL-CR-00521, Nov 83.
13. Cambel, A.B. Plasma Physics and Magnetofluidmechanics (McGraw-Hill, New York, 1963), Chap. 7.
14. Barber, J.P., private communication.

DISTRIBUTION LIST

<u>No. of Copies</u>	<u>Organization</u>	<u>No. of Copies</u>	<u>Organization</u>
12	Administrator Defense Technical Info Center ATTN: DTIC-DDA Cameron Station Alexandria, VA 22304-6145	1	Director US Army Aviation Research and Technology Activity Ames Research Center Moffett Field, CA 94035-1099
1	HQDA (SARD-TR) Washington, DC 20310		
1	Commander US Army Material Command ATTN: AMCDRC-ST 5001 Eisenhower Avenue Alexandria, VA 22333-0001	1	Commander US Army Missile Command ATTN: AMSMI-RD-CS-R (DOC) Redstone Arsenal, AL 35898-5241
1	Commander US Army Laboratory Command ATTN: AMSLC-DL 2800 Powder Mill Road Adelphi, MD 20783-1145		
1	Commander Armament R&D Center US Army AMCCOM ATTN: SMCAR-MSI Picatinny Arsenal, NJ 07806-5000	1	Director DARPA ATTN: Dr. Peter Kemmey 1400 Wilson Blvd. Arlington, VA 22209
3	Commander US Army Armament R&D and Engineering Center ATTN: SMCAR-TDC SMCAR-SCA-E (Mr. H. Kahn) DRDAR-LCA-C (Dr. T. Gora) Picatinny Arsenal, NJ 07806-5000	1	Commander US Army Tank Automotive Command ATTN: AMSTA-TSL Warren, MI 48397-5000
2	Director Benet Weapons Laboratory ATTN: SMCAR-LCB-TL SMCAR-LCB-DS (Dr. C.A. Andrade) Watervliet, NY 12189	1	Director US Army TRADOC Analysis Command ATTN: ATAA-SL White Sands Missile Range, NM 88002 -5502
1	Commander US Army Armament, Munitions and Chemical Command ATTN: SMCAR-ESP-L Rock Island, IL 61299	1	Commandant US Army Infantry School ATTN: ATSH-CD-CSO-OR Fort Benning, GA 31905 -5660
1	Commander US Army Aviation System Command ATTN: AMSAV-DACL 4300 Goodfellow Blvd. St. Louis, MO 63120	2	Commander SDIO ATTN: SDIO/IST (MAJ M. Huebschman) (Dr. Dwight Duston) Washington, DC 20301-7100

DISTRIBUTION LIST

<u>No. of Copies</u>	<u>Organization</u>	<u>No. of Copies</u>	<u>Organization</u>
1	Director US Army Research Office ATTN: Dr. Michael Cifan Research Triangle Park, NC 27709-2211	3	Maxwell Laboratories ATTN: Dr. Rolf Dethlefsen Dr. Michael M. Holland Dr. Mark Wilkinson 8888 Balboa Avenue San Diego, CA 92123
1	AFWL/SUL Kirkland AFB, NM 87117	1	Boeing Aerospace Company ATTN: Dr. J.E. Shrader P.O. Box 3999 Seattle, WA 98134
5	Air Force Armament Laboratory ATTN: AFATL/DLODL AFATL/DLJG (Mr. Kenneth Cobb) AFATL/DLYS (LT Jeff Martin) AFATL/DLDG (Dr. T. Aden) AFATL/SAS (CAPT J. Scanlon) Eglin AFB, FL 32542-5000	2	GA Technologies, Inc. ATTN: Dr. Robert Bourque Dr. L. Holland P.O. Box 85808 San Diego, CA 92138
1	Director Brookhaven National Laboratory ATTN: Dr. J.R. Powell, Bldg 129 Upton, NY 11973	2	GT Devices ATTN: Dr. Shyke Goldstein Dr. Y.C. Thio 5705-A General Washington Drive Alexandria, VA 22312
1	Director Lawrence Livermore National Laboratory ATTN: Dr. R.S. Hawke, L-156 P.O. Box 808 Livermore, CA 94550	1	General Dynamics ATTN: Dr. Jaime Cuadros P.O. Box 2507 Pomona, CA 91766
3	Director Los Alamos National Laboratory ATTN: MSG 787. (Mr. Max Fowler) Dr. J.V. Parker Dr. William Condit Los Alamos, NM 87545	2	Electromagnetic Research, Inc ATTN: Dr. Henry Kolm Dr. Peter Mongeau 2 Fox Road Hudson, MA 01749
1	Sandia National Laboratory ATTN: Dr. Maynard Cowan, Dept 1220 P.O. Box 5800 Albuquerque, NM 87185	2	General Electric Company (AEPD) ATTN: Dr. William Bird Dr. Slade L. Carr R.D. #3, Plains Road Ballston Spa, NY 12020
1	NASA Lewis Research Center ATTN: MS 501-7 (Lynette Zana) 2100 Brook Park Road Cleveland, OH 44135	1	General Research Corporation ATTN: Dr. William Isbell 5383 Hallister Avenue Santa Barbara, CA 93111
1	Astron Research & Engineering ATTN: Dr. Charles Powars 130 Kifer Court Sunnyvale, CA 94086	1	Gould Defense Systems, Inc. Oceans Systems Division ATTN: Dr. Donald M. McEligot One Corporate Place Newport Corporate Park Middleton, RI 02840
2	Austin Research Associates ATTN: Dr. Millard L. Sloan Dr. William E. Drummond 1091 Rutland Drive Austin, TX 78758		

DISTRIBUTION LIST

<u>No. of Copies</u>	<u>Organization</u>	<u>No. of Copies</u>	<u>Organization</u>
2	IAP Research, Inc. ATTN: Dr. John P. Barber Mr. David P. Bauer 2763 Culver Avenue Dayton, OH 45429-3723	2	Auburn University ATTN: Dr. Raymond F. Askew Leach Nuclear Science Center Dr. E.J. Clothiaux Department of Physics Auburn University, AL 36849-3501
1	LTV Aerospace & Defense Company ATTN: Dr. Michael M. Tower Dr. C.H. Haight, MS TH-83 P.O. Box 650003 Dallas, TX 75265-0003	1	Texas Technical University Department of EE/Computer Science ATTN: Dr. M. Kristiansen Lubbock, TX 79409-4439
1	Pacific-Sierra Research Corp. ATTN: Dr. Gene E. McClellan 1401 Wilson Blvd. Arlington, VA 22209	1	Tuskegee Institute Department of Mechanical Engineering ATTN: Dr. Pradosh Ray Tuskegee Institute, AL 36088
2	Physics International Company ATTN: Dr. A.L. Brooks Dr. Frank Davies 2700 Merced Street San Leandro, CA 94577	1	University of Alabama in Huntsville School of Science & Engineering ATTN: Dr. C.H. Chen Huntsville, AL 35899
1	R&D Associates ATTN: Dr. Peter Turchi P.O. Box 9695 Marina del Rey, CA 90291	1	University of Miami ATTN: Dr. Manuel A. Huerta Physics Department P.O. Box 248046 Coral Gables, FL 33124
3	SAIC ATTN: Dr. Jad H. Batteh Dr. G. Rolader Mr. L. Thornhill 1503 Johnson Ferry Road, Suite 100 Marietta, GA 30062	1	University of Tennessee Space Institute ATTN: Dr. Dennis Keefer Tullahoma, TN 37388-8897
1	System Planning Corporation ATTN: Donald E. Shaw 1500 Wilson Blvd. Arlington, VA 22209	3	University of Texas Center for Electromechanics Balcones Research Center ATTN: Mr. William Weldon Mr. Raymond Zaworka Dr. Harry Fair 10100 Burnet Road, Bldg. 133 Austin, TX 78748
2	Westinghouse Electric Corporation Marine Division ATTN: Dr. Dan Omry Dr. Ian R. McNab 401 East Hendy Avenue Sunnyvale, CA 94088-3499	1	Dr. E.W. Sucoy 1065 Lyndhurst Drive Pittsburgh, PA 15206
1	Westinghouse R&D Laboratory ATTN: Dr. Bruce Swanson 1310 Beulah Road Pittsburgh, PA 15233		

DISTRIBUTION LIST

**No. of
Copies Organization**

**No. of
Copies Organization**

Aberdeen Proving Ground

Dir, USAMSAA
ATTN: AMXSY-D
 AMXSY-MP, H. Cohen

Cdr, USATECOM
ATTN: AMSTE-SI-F

Cdr, CRDC, AMCCOM
ATTN: SMCCR-RSP-A
 SMCCR-MU
 SMCCR- MSI

USER EVALUATION SHEET/CHANGE OF ADDRESS

This laboratory undertakes a continuing effort to improve the quality of the reports it publishes. Your comments/answers below will aid us in our efforts.

1. Does this report satisfy a need? (Comment on purpose, related project, or other area of interest for which the report will be used.) _____

2. How, specifically, is the report being used? (Information source, design data, procedure, source of ideas, etc.) _____

3. Has the information in this report led to any quantitative savings as far as man-hours or dollars saved, operating costs avoided, or efficiencies achieved, etc? If so, please elaborate. _____

4. General Comments. What do you think should be changed to improve future reports? (Indicate changes to organization, technical content, format, etc.) _____

BRL Report Number _____ Division Symbol _____

Check here if desire to be removed from distribution list. _____

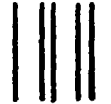
Check here for address change. _____

Current address: Organization _____
Address _____

-----FOLD AND TAPE CLOSED-----

Director
U.S. Army Ballistic Research Laboratory
ATTN: SLCBR-DD-T (NEI)
Aberdeen Proving Ground, MD 21005-5066

OFFICIAL BUSINESS
PENALTY FOR PRIVATE USE \$300



NO POSTAGE
NECESSARY
IF MAILED
IN THE
UNITED STATES

BUSINESS REPLY LABEL
FIRST CLASS PERMIT NO. 12062 WASHINGTON D. C.
POSTAGE WILL BE PAID BY DEPARTMENT OF THE ARMY



Director
U.S. Army Ballistic Research Laboratory
ATTN: SLCBR-DD-T (NEI)
Aberdeen Proving Ground, MD 21005-9989